



# Transverse Isotropy of Phyllite Under Brazilian Tests: Laboratory Testing and Numerical Simulations

Guowen Xu<sup>1</sup> · Chuan He<sup>1</sup> · Ziquan Chen<sup>1</sup> · Ang Su<sup>1</sup>

Received: 8 April 2017 / Accepted: 22 December 2017 / Published online: 29 December 2017  
© Springer-Verlag GmbH Austria, part of Springer Nature 2017

## Abstract

Phyllite is a low-grade, metamorphic rock with well-developed foliation. We characterized the fracture pattern and failure strength of phyllite specimens under Brazilian tests. The specimens were obtained from the Zhegu mountain tunnel in China and had different foliation-loading angles, namely 0°, 15°, 30°, 45°, 60°, 75° and 90°. The processes for the initiation and propagation of macro-cracks were recorded using high-speed photography. The evolution of micro-cracks was analyzed based on the results of acoustic emission (AE) tests. The failure process of the specimens during the Brazilian tests was simulated with a new numerical approach based on the particle discrete element method. The influence of foliation strength and the microstructure of the rock matrix were also studied numerically. The experimental results showed that the failure strength of the specimens was related to their fracture patterns and the areas of their fracture surfaces. The initial cracking point of the specimens appeared at the upper or lower loading position, and the cracks propagated to the boundaries of the specimens along or across foliation. The temporal distributions of the AE counts and AE energy of the specimens were affected predominantly by the fracture pattern, and we divided these distributions into two modes: the peak mode and the uniformly distributed mode. The numerical results indicated that the fracture surface was roughly parallel to the loading direction and that the surface was located in the central part of the disk specimens for rocks with loose structure (low coordination number or large crack density) or with strong foliation, i.e., foliation with high shear strength. The failure pattern and trends of variation in failure strength as a function of foliation-loading angles varied with the ratio of cohesion to the tensile strength of foliation, the crack density, and the coordination number.

**Keywords** Transverse · Isotropy · Brazilian tests · High-speed photography · Acoustic emission tests · Particle discrete element

## List of symbols

|                  |   |                    |   |
|------------------|---|--------------------|---|
| $\sigma_t$       | Tensile strength (Pa)                                     | $k^n$              | Normal stiffness of particle (Pa m <sup>-1</sup> )          |
| $F$              | Peak loading force (N)                                    | $k^s$              | Shear stiffness of particle (Pa m <sup>-1</sup> )           |
| $D$              | Diameter of rock specimen (m)                             | $\mu_c$            | Friction coefficient between particles                      |
| $t$              | Thickness of rock specimen (m)                            | $g_{\text{ratio}}$ | Installation gap ratio                                      |
| $U$              | Energy of AE signal (J)                                   | $\varphi_S$        | Slit element fraction                                       |
| $R$              | Input impedance of preamplifier ( $\Omega$ )              | $\bar{k}_n$        | Normal stiffness of smooth joint bond (Pa m <sup>-1</sup> ) |
| $V$              | Voltage of AE signal (V)                                  | $\bar{k}_s$        | Shear stiffness of smooth joint bond (Pa m <sup>-1</sup> )  |
| $\bar{\sigma}_c$ | Normal strength of flat-joint bond (Pa)                   | $\bar{\lambda}$    | Radius multiplier   |
| $\bar{\tau}_c$   | Shear strength of flat-joint bond (Pa)                    | $\mu$              | Friction coefficient of smooth joint bond                   |
| $\bar{k}^n$      | Normal stiffness of flat-joint bond (Pa m <sup>-1</sup> ) | $\sigma_c$         | Normal strength of smooth joint bond (Pa)                   |
| $\bar{k}^s$      | Shear stiffness of flat-joint bond (Pa m <sup>-1</sup> )  | $c_b$              | Cohesion of smooth joint bond (Pa)                          |
|                  |   | $\varphi_b$        | Friction angle between particles (°)                        |

✉ Guowen Xu  
xgw80033@163.com

<sup>1</sup> Key Laboratory of Transportation Tunnel Engineering, Ministry of Education, Southwest Jiaotong University, Chengdu 610031, Si Chuan, China

## 1 Introduction

Sedimentary or metamorphic rocks always contain weak planes (bedding planes, foliation, schistosity, or jointing). These fabric structures are the source of the transverse isotropy of rocks (Kim et al. 2012; Khanlari et al. 2014) and strongly influence the stability of geotechnical engineering projects, such as underground excavation (Blümling et al. 2007; Lisjak et al. 2016), the storage of radioactive substances (Tsang et al. 2012; Valente et al. 2012), and drilling for petroleum (Martin et al. 2012). In engineering projects, rock material is vulnerable to damage in tension because of its low tensile strength, prompting the development of the Brazilian test method (Barla and Innaurato 1973) to measure the tensile strength of transversely isotropic rocks. Since that time, interest in transverse isotropy of tensile strength has increased significantly, and numerous research results have been obtained using this method.

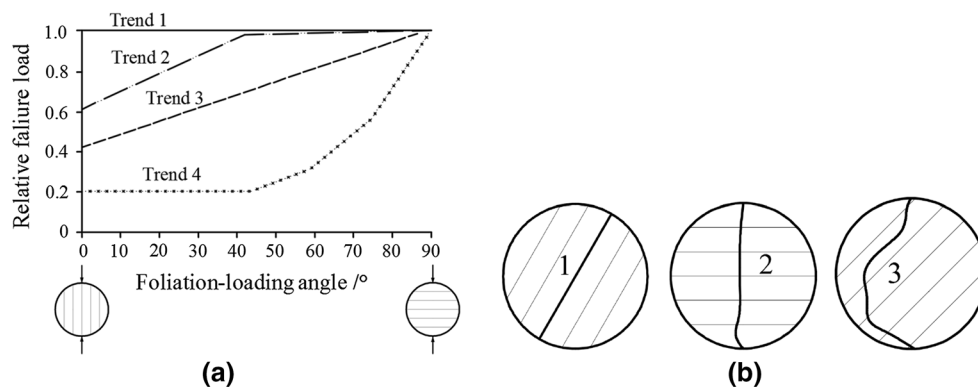
In a theoretical study, Amadei et al. (1983) derived an analytical solution of tensile strength for transversely isotropic rock based on the method proposed by Lekhnitskii (1968). Several years later, a semi-analytical solution of tensile strength and Young's modulus for transversely isotropic rock was developed by Chen et al. (1998). In the numerical approach, the discrete element method (DEM) has been used extensively because weak planes can be embodied intuitively in this method. The block DEM was adopted by Debecker (2009) and Tan et al. (2015) to investigate the failure of slate and Mosel slate during Brazilian tests. Using particle DEM, Park and Min (2015) and Duan and Kwok (2015) succeeded in simulating the mechanical behavior of induced and inherent transversely isotropic rock.

Numerous experimental results from laboratory tests have been published, including those on sandstone (Chen et al. 1998; Tavallali and Vervoort 2010; Vervoort et al. 2014), slate (Dan 2011; Liu 2013), shale (Cho et al. 2012; Yang

et al. 2015a, b), schist (Cho et al. 2012), and gneiss (Dan 2011; Cho et al. 2012; Roy and Singh 2016). These results indicate that weak planes can have a significant effect on the strength and fracture pattern of rocks, with the extent of the effect depending on the type of rock. Vervoort et al. (2014) obtained four different trends in variation of the relative failure load as a function of inclination angle from nine different rocks (Fig. 1a). Tavallali and Vervoort (2010) obtained three different fracture patterns from their test results with sandstone (Fig. 1b). Researchers have attempted to capture the initiation and propagation process of cracks. Debecker (2009) recorded the evolution process of cracks in slate specimens at a lower loading speed (0.05 mm/min) using a digital camera. Yang et al. (2015a, b) found that the initial cracking point of shale occurred approximately at the loading position and that the cracks propagated from the two ends of the specimen to the middle.

In previous research, the microstructure of the rock matrix (pre-existing cracks, contact state of particles) has not been considered in numerical simulations, and little attention has been paid to the mesoscopic fracture mechanism of experimental specimens. Therefore, in this paper, we present a combination of experimental and numerical methods to study the fracture mechanisms of carbonaceous phyllite at the macroscopic and mesoscopic levels. This focus is important because fracture of phyllite occurs frequently during the construction of high-speed railways and highways in western China. The failure strength and fracture patterns, initiation and propagation processes of macro-cracks, and the generation and evolution of micro-cracks were obtained through Brazilian tests of the specimens at different foliation-loading angles. A new numerical approach was developed to study the deformation and failure process of rocks. In addition, the impacts of the strength parameters of weak planes and the microstructure of the rock matrix on the macro-mechanical behavior of rock are discussed in detail.

**Fig. 1** Summary of Brazilian test results of transversely isotropic rocks: **a** four different trends in the variation of the relative failure load as a function of the foliation-loading angle (after Vervoort et al. 2014); **b** three different fracture patterns (after Tavallali and Vervoort 2010) (1: layer activation; 2: central fracture; 3: non-central fracture)



## 2 Test Preparation

### 2.1 Preparation of Rock Specimen

As shown in Fig. 2, phyllite specimens were obtained from the Zhegu mountain tunnel, which is located on the highway between Wenchuan and Barkam, Sichuan Province, China. The tunnel is a two-way, four-lane separated tunnel with a length of 8784 m, a width of 13.4 m, a height of 10.5 m, and a maximum depth of 1300 m.

The results of X-ray diffraction indicated that the main minerals in the phyllite specimens were illite, chlorite, quartz, and plagioclase, which accounted for 40, 33, 19, and 8% of the total mass, respectively, as illustrated in Fig. 3. Well-developed foliation can be observed in the SEM images (Fig. 4).

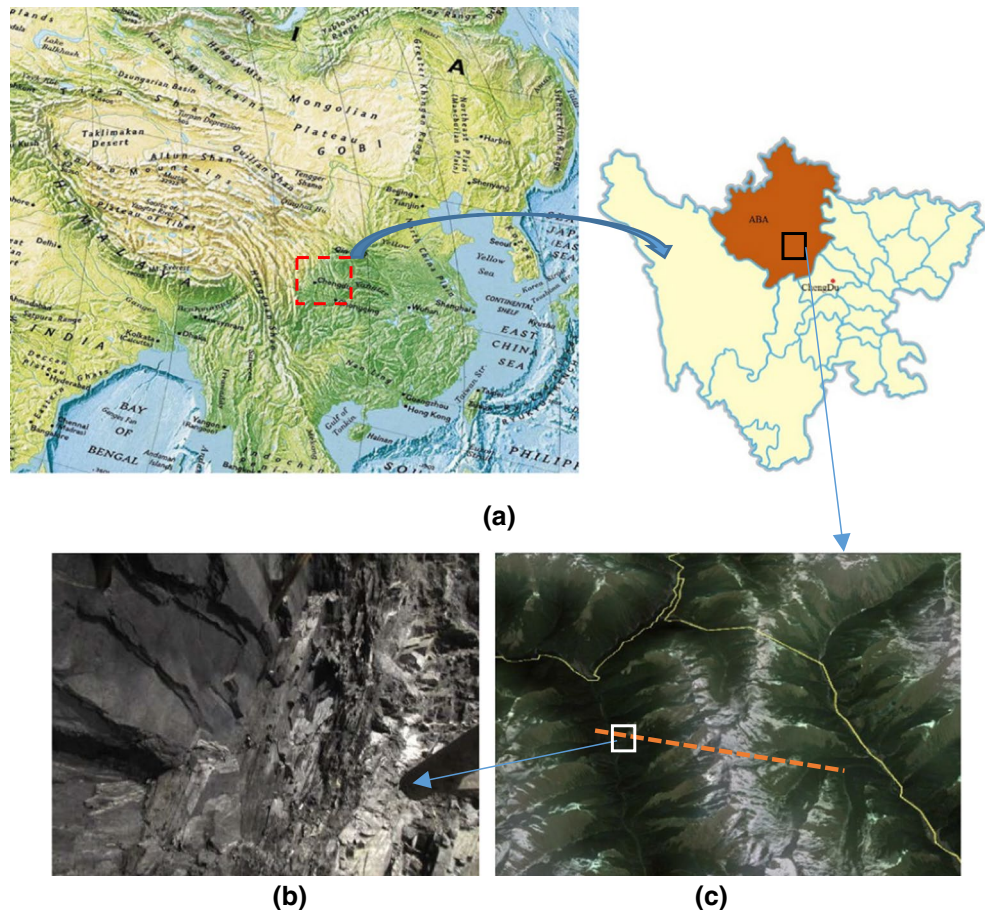
The process used to prepare the disk-shaped specimens is shown in Fig. 5. First, cylindrical specimens with diameters of 50 mm were obtained by core drilling along the direction parallel to the weak planes. Then, the specimens were cut using a high-speed cutting machine into several disks measuring 50 mm × 25 mm; the ratio of the length

to the diameter was 0.5. The surfaces of all the disks were ground using a grinding machine to ensure flatness.

### 2.2 Test Procedure

The layout of the test devices is shown in Figs. 6 and 7. The tests were conducted using an electronic universal testing machine whose maximal axial loading capacity was 100 kN, with ± 0.5% accuracy in the measurements of force and deformation. The acoustic emission (AE) signals generated during the loading process were recorded by a PCI-2 AE detection system developed by the American Physical Acoustics Corporation. Two AE sensors were placed at point A and B on disk specimen, as shown in Fig. 7. The AE sensors are Mic 30 sensors with a resonant frequency of 200 kHz and a recording frequency ranged from 20 kHz to 1 MHz. The detection threshold of the signal was 40 dB. The time parameters, i.e., peak definition time (PDT), hit definition time (HDT), and hit locking time (HLT), were 50, 200, and 300 s, respectively. A high-speed camera was used to record the propagation process of macro-cracks. For each specimen, the surface on which the AE sensor was installed was called surface A, and the surface facing the high-speed camera was called surface B.

**Fig. 2** Site of rock sampling: **a** tunnel location; **b** tunnel face; **c** tunnel longitudinal axis



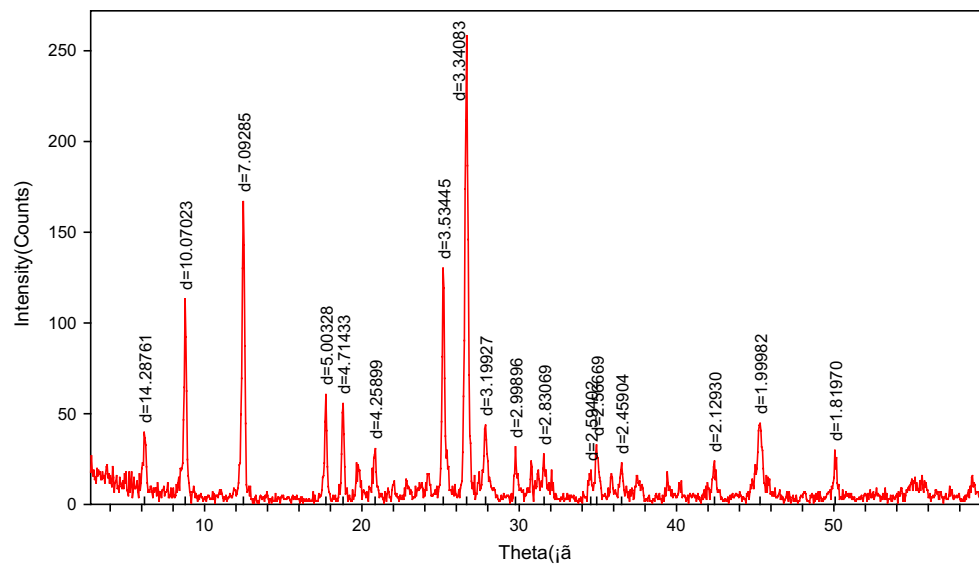


**Fig. 3** X-ray diffraction result of rock powders

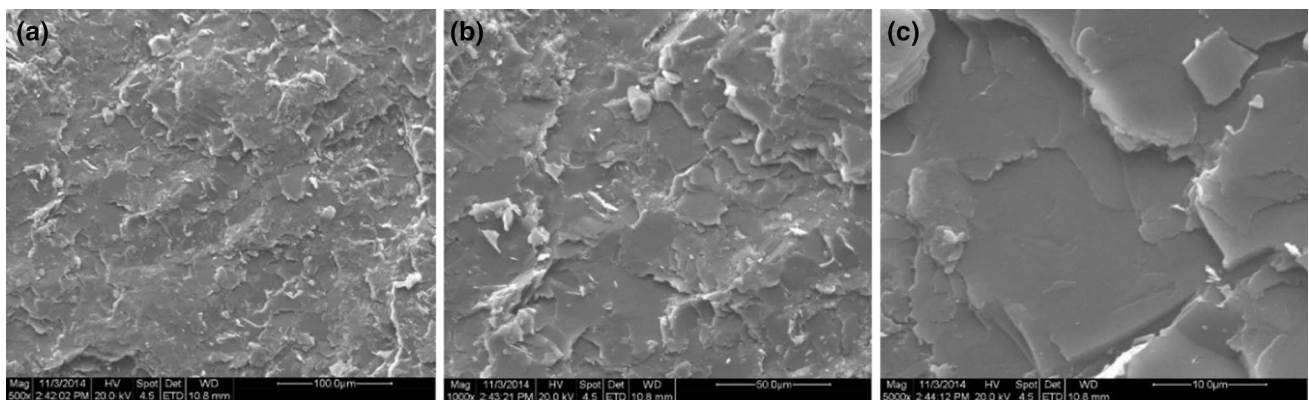


**Fig. 4** SEM micrographs: **a**  $\times 500$ ; **b**  $\times 1000$ ; **c**  $\times 5000$

**Fig. 5** Process of preparing the disk specimens

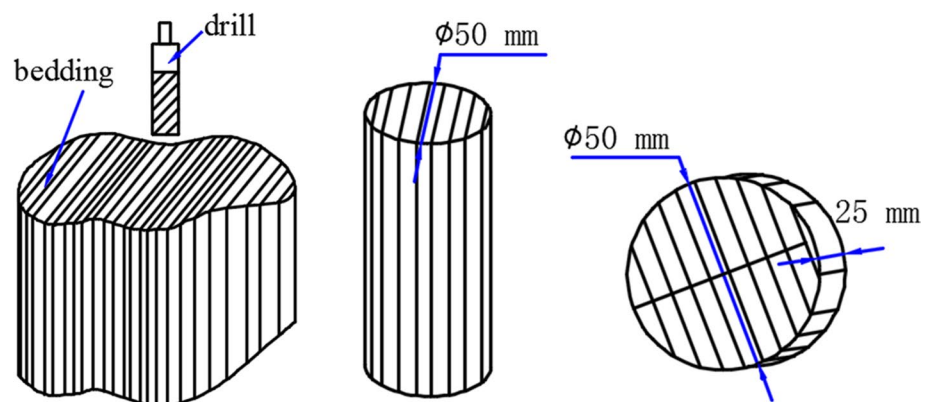






Fig. 6 Layouts of the test devices

Seven foliation-loading angles, namely,  $\theta = 0^\circ, 15^\circ, 30^\circ, 45^\circ, 60^\circ, 75^\circ$  and  $90^\circ$ , were chosen to investigate the transversely isotropic behavior of phyllite in this test, as shown in Fig. 7. Five specimens were used for each angle to accommodate outlier results. The loading process was conducted with an increasing axial load at a constant rate of 100 N/s until the specimens failed.

Fig. 7 Scheme of foliation-loading angle during the tests: a  $\theta = 0^\circ$ ; b  $0^\circ < \theta < 90^\circ$ ; c  $\theta = 90^\circ$ . (1: bearing plate; 2: disk specimen; 3: stiff wire; 4: foliation; 5: AE sensors)

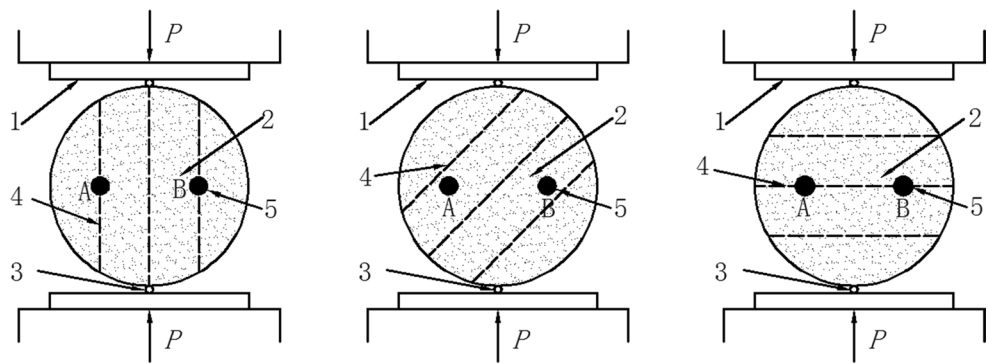


Table 1 Failure strength of specimens/MPa

| $\theta$    | $0^\circ$ | $15^\circ$ | $30^\circ$ | $45^\circ$ | $60^\circ$ | $75^\circ$ | $90^\circ$ |
|-------------|-----------|------------|------------|------------|------------|------------|------------|
| Specimen 1# | 2.29      | 3.02       | 2.89       | 2.71       | 3.75       | 5.23       | 10.00      |
| Specimen 2# | 1.91      | 1.34       | 2.57       | 2.32       | 2.37       | 5.45       | 19.53      |
| Specimen 3# | 1.75      | 1.72       | 3.68       | 5.28       | 1.72       | 7.75       | 4.70       |
| Specimen 4# | 2.55      | 1.17       | 2.36       | 3.65       | 2.25       | 7.21       | 18.00      |
| Specimen 5# | 2.33      | 1.67       | 2.40       | 3.26       | 2.66       | 5.15       | 7.24       |
| Average     | 2.16      | 1.78       | 2.78       | 3.44       | 2.55       | 6.16       | 11.89      |

The name of specimen is composed of two items, representing foliation-loading angle  $\theta$  and number in sequential order. For example, N0-1 denotes the specimen 1# with  $\theta = 0^\circ$

### 3 Test Results

#### 3.1 Failure Strength

The formula for tensile strength is expressed in Eq. (1):

$$\sigma_t = \frac{2F}{\pi Dt}, \tag{1}$$

where  $\sigma_t$  is the tensile strength,  $F$  is the peak loading force,  $D$  is the diameter of the specimen, and  $t$  is the thickness of the specimen. Two requirements must be met for this formula to be used, namely (1) the specimen must be isotropic and (2) the fracture pattern should be initiated by tensile failure from the center of the specimen. Thus, for transversely isotropic rock, the strength obtained from the formula is not always equal to its tensile strength. We used this formula in our work to eliminate the influence of the diameter and thickness on the peak loading force. Thus, we use the term “failure strength” instead of “tensile strength” to describe the results of the calculations.

The maximum failure strength was 11.89 MPa when  $\theta$  was  $90^\circ$ , and this strength decreased sharply to 2.55 MPa at  $\theta = 60^\circ$ ; it then leveled off, as indicated in Table 1, indicating that the trend in the variation of failure strength with foliation-loading angles of phyllite is “trend IV” according to the definition provided by Vervoort et al. (2014) (Fig. 1a).

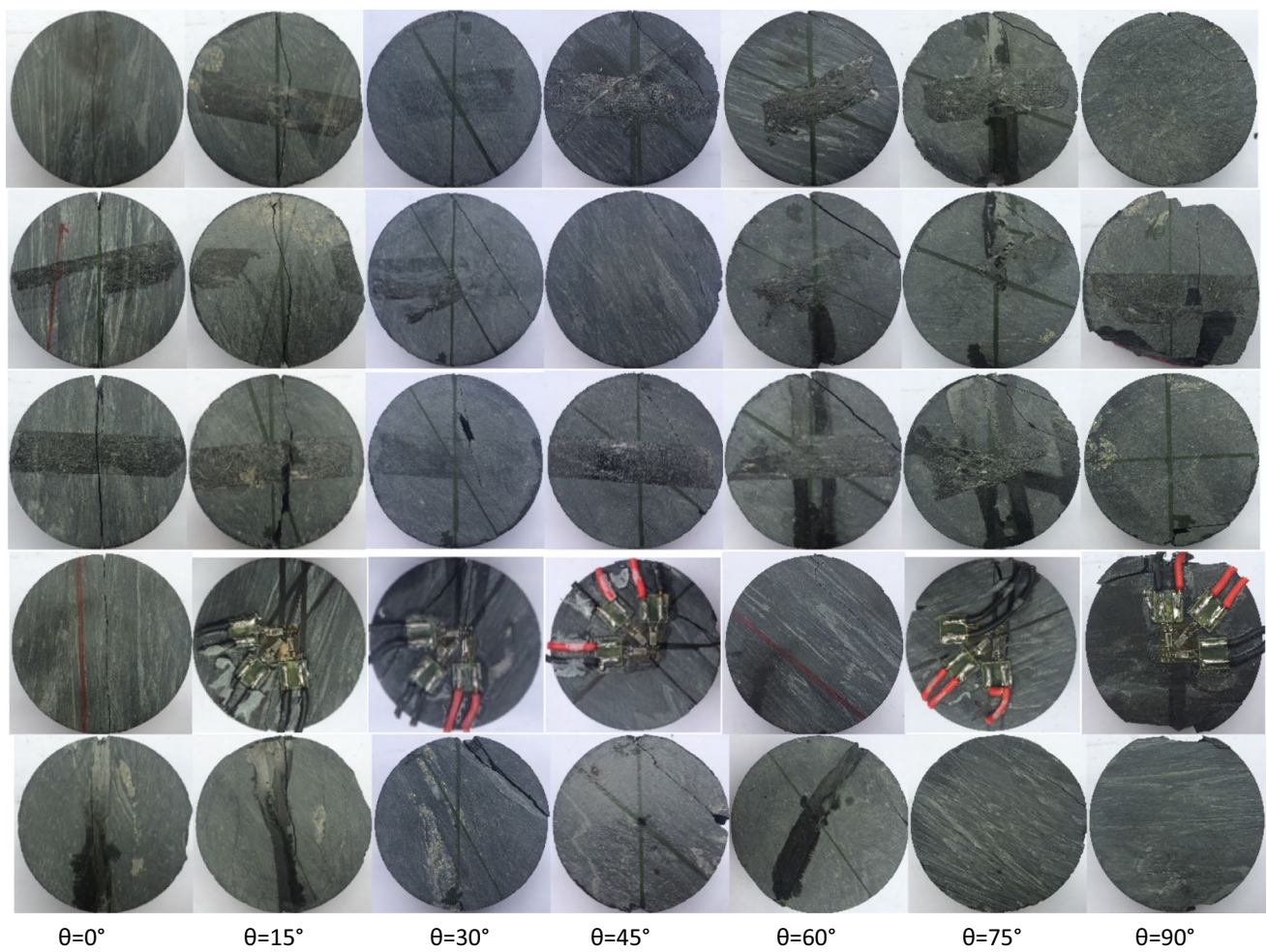


**Fig. 8** Fracture patterns at different foliation-loading angles (surface A)

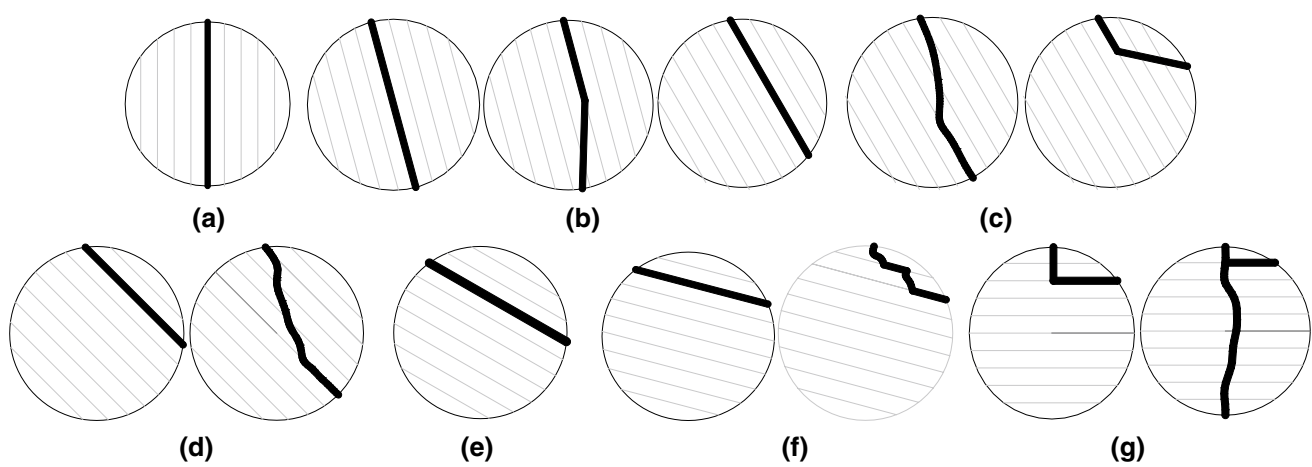


**Fig. 9** Sketches of fracture patterns: **a**  $\theta = 0^\circ$ ; **b**  $\theta = 15^\circ$ ; **c**  $\theta = 30^\circ$ ; **d**  $\theta = 45^\circ$ ; **e**  $\theta = 60^\circ$ ; **f**  $\theta = 75^\circ$ ; **g**  $\theta = 90^\circ$

### 3.2 Fracture Pattern

The fracture pattern was essentially two-dimensional, in most cases being similar on surface A and B. Therefore, only the fracture pattern on surface A is presented in this paper. Figures 8 and 9 display the pictures and sketches, respectively, of the ultimate fracture patterns for the specimens at different  $\theta$ . The figures show that the fracture patterns can be divided into three types: layer activation failure (type I), mixed failure (type II), and non-layer activation failure (type III). As shown in Fig. 9, the fracture patterns of the specimens were type I at  $\theta = 0^\circ$  or  $\theta = 60^\circ$ , type II or type III at  $\theta = 90^\circ$ , and type I or type II at other foliation-loading angles.

As shown in Table 1, the failure strengths of the five specimens at the same  $\theta$  value were separate and distinct, which was related to their fracture patterns. Taking  $\theta = 30^\circ$  as an example, the fracture patterns of specimens 3 and 1 were type II, with the fracture surfaces located mainly across or along the foliations, respectively. Their corresponding failure strengths were 3.68 and 2.89 MPa, which were the largest and second largest among the five specimens. The failure strengths of specimens 2 and 4 were lower than specimens 3 and 1 due to their layer activation failures. Although the fracture pattern of specimen 5 was the same as that of specimen 3, its failure strength was almost equal to that of specimens 2 and 4 due to the smaller fracture surface. The same conclusion can be obtained at the other  $\theta$  values. This phenomenon will be explained in Sect. 4.2 based on the results of the AE tests.

## 4 Failure Process of Phyllite

### 4.1 Results of High-Speed Photography

The initiation point of cracks and their propagation process are of interest in the Brazilian test. In this study, the failure process of the specimens (Fig. 10) was recorded by a high-speed camera with a speed of 20,000 frames per second. The photographs indicated that the initial cracking points were at the upper or lower loading position and that the cracks propagated along or across foliation to the boundaries of the specimens. The specific process for the evolution of cracks for each foliation-loading angle is described below.

For  $\theta = 0^\circ$ , two evolutionary processes were observed. A crack appeared in specimen N0-1 (Fig. 10a) at the upper loading position that propagated downward along the foliation. The primary crack of specimen N0-4 (Fig. 10b) initiated at the lower loading position and propagated upward along the foliation. The secondary crack was observed near the upper loading position, and it propagated along the

foliation to some extent during the evolution of the primary crack.

For  $\theta = 15^\circ$ , the crack in specimen N15-2 (Fig. 10c) was observed at the upper loading position. It developed along the foliation to point 1 and then propagated downward in a direction parallel to the axial loading stress. The crack in specimen N15-5 (Fig. 10d) initiated at the upper loading position; it propagated downward along the direction of the loading stress to point 1, after which it propagated along the foliation to point 2. A new crack appeared at the lower loading position and propagated to point 3. The two cracks coalesced to form one main crack as the loading stress was increased.

For  $\theta$  values in the range of  $30^\circ$ – $75^\circ$ , the dominant fracture pattern is type I. Taking specimen N45-2 as an example, its main crack started at the upper loading position and propagated along the foliation to the boundary of the specimen.

The failure process for N90-2 is shown in Fig. 10f. The specimen broke near the upper loading point; the crack propagated downward along a curved track until it reached the lower loading point.

For transversely isotropic rock, the propagation process of cracks is determined by the foliation-loading angle. Other parameters, such as the strength of foliation and the microstructure of the rock matrix, also have a significant influence on specimens that undergo different fracture paths with the same angle. However, the influence of the microstructure and foliation strength is challenging to examine experimentally; thus, this influence is systematically examined in Sect. 5 using numerical simulation.

To meet the image definition and sampling frequency, the high-speed camera with the ring acquisition pattern can record the test process for only 8 s in this experiment. Thus, new data will automatically overwrite the original data every 8 s. For specimen N90-2, the loading process was lengthy and the high-speed camera was unable to record the entire failure process. Thus, in Fig. 10f, the failure process near the upper loading point is missing. Therefore, in the process of rock failure, when the phase of the initial crack, i.e., initiation, propagation, or coalescence, is unambiguous and when the loading time is long, a digital camera can be used to compensate for the limitations of the high-speed camera (Debecker 2009).

### 4.2 Results of the AE Test

Many micro-cracks occur during the loading process, and their generation is accompanied by the release of sound waves and energy. The record of this information enables a better understanding of the fracture process of rock on the mesoscopic level (Lockner 1993). The AE energy is influenced by fracture types of micro-cracks and orientation of sensors to the source. Thus, in order to reduce the influence



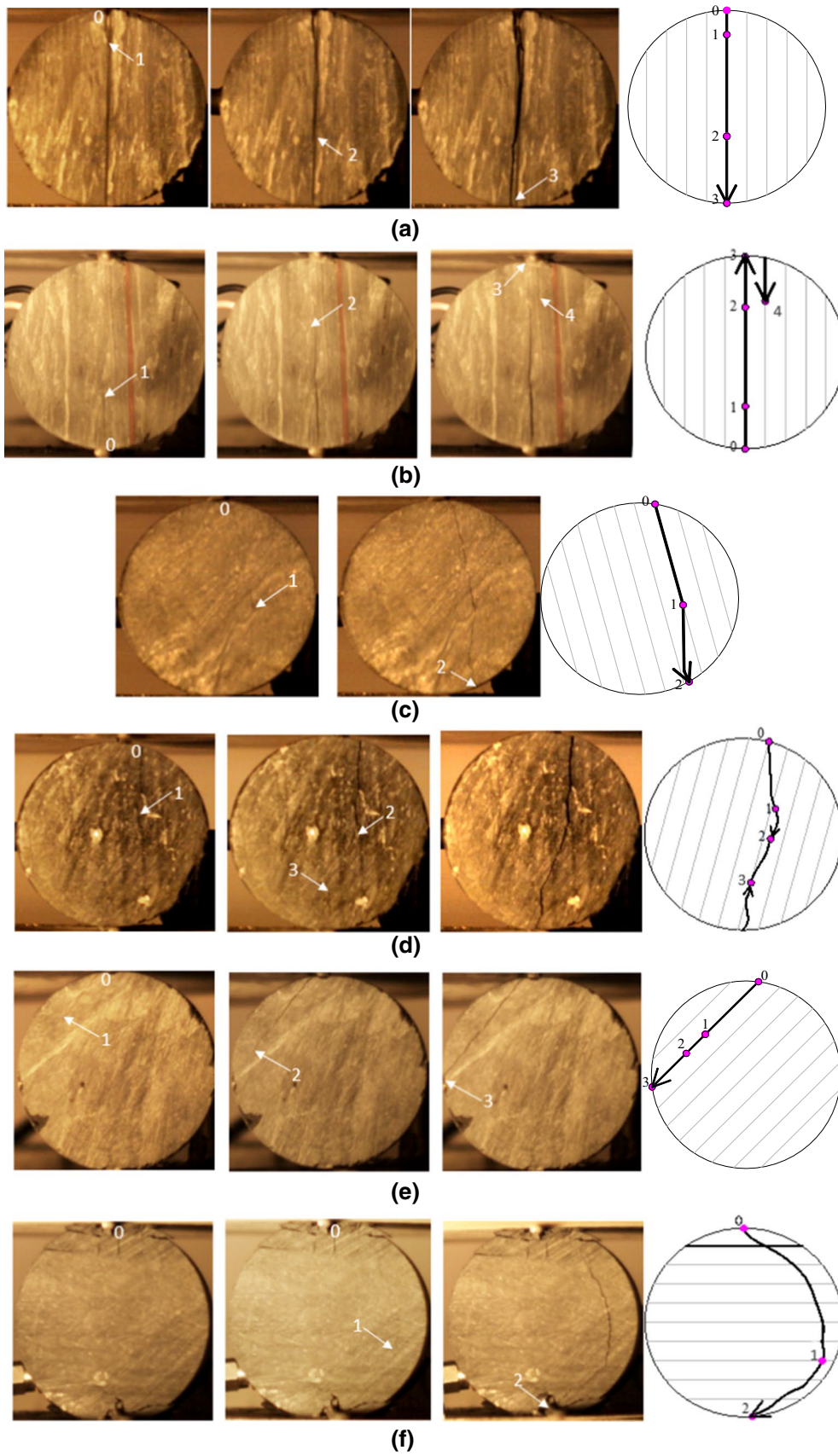




**Fig. 10** High-speed photography of failure process: **a** N0-1; **b** N0-4; **c** N15-2; **d** N15-5; **e** N45-2; **f** N90-2 (0 denotes initial cracking point; 1, 2 and 3 denote the captured points at the crack propagation path)

of the aforementioned factors, we choose the maximum value of energy between signals recorded by sensors at point A and point B to analyze the evolution of micro-cracks. It is worth noting that, for transversely isotropic rocks, the fracture patterns are diverse, resulting in the difference of energy attenuation for specimens with different macroscopic fracture patterns and quantifying this difference needs much work to be done.

Figure 11 displays the relationship between the AE counts, AE energy, and strain for different values of  $\theta$ . The AE energy is based on the sum of squared voltage divided by a resistance  $R$  (Pollock 2013) as shown in Eq. (2):

$$U = \frac{1}{R} \sum_{FTC}^{PDT} V_i^2 \Delta t \tag{2}$$

where the value of  $R$  is 10 k $\Omega$  denoting the input impedance of the preamplifier, FTC represents “First Threshold Crossing.” The energies were reported in attojoules (aJ = 10<sup>-18</sup> J).

The mode of the AE count rate curve and energy rate curve during the entire loading period can be divided into two modes: (1) M-I, the peak distribution mode, which is the distribution of the AE count rate or energy rate presents 1, 2 or finite peak intervals during the loading process; and (2) M-II, the uniform distribution mode. That is, the distribution of the AE count rate or energy rate is uniform during the loading process. The modes of the AE characteristic curves (AE count rate curve and the energy rate curve, “curves” for simplicity) are summarized in Table 2. Note that the modes are not divided strictly and that there is a transition over the two modes.

Figure 11 and Table 2 show that the mode of the curves is related to  $\theta$  and the fracture pattern, resulting in the following features:

1. When  $\theta$  is small (e.g.,  $\theta = 0^\circ$  or  $15^\circ$ ), the fracture pattern has no effect on the modes of curves. Curves for  $\theta = 0^\circ$  are categorized as M-I and present a bimodal distribution. The first peak point is located at the transition position from the slow growth of stress to fast growth, and the second peak point is located near the peak stress. Curves for  $\theta = 15^\circ$  are categorized as M-I and present unimodal distributions. The peak point appears near the peak stress.
2. For  $\theta$  values in the range of  $30^\circ$ – $75^\circ$ , when the fracture pattern is type I, a transition exists from a multimodal distribution ( $\theta = 30^\circ, 45^\circ$ ) to a unimodal distribution ( $\theta = 60^\circ, 75^\circ$ ) for the AE energy rate curves. The AE count rate curves have unimodal distributions except for

$\theta = 60^\circ$ . When the fracture pattern is type II, both the AE energy rate and the count rate are distributed uniformly during the entire loading process.

3. For  $\theta = 90^\circ$ , irrespective of whether the fracture pattern is type II or type III, the curves belong to M-I and have multimodal distributions.

The AE test results indicate that the AE characteristic curves always present unimodal or bimodal distributions when the failure pattern is layer activated, indicating that damage occurs at the high-stress level after the specimens have accumulated sufficient energy and that the rock is more prone to brittle failure in this condition. When the failure pattern of specimens is in the form of non-layer activation and mixed failure, the AE characteristic curves always present multimodal or uniform distributions, indicating that the micro-cracks occurred during the initial loading stage and propagated during the entire loading process, making the rock more prone to plastic failure.

In most cases with the same  $\theta$  value, when the fracture pattern is type I, the AE activity is weaker than for type II or type III. Taking  $\theta = 45^\circ$  for example, when the fracture pattern is type I, the AE count is 271, and the released energy is  $4.78 \times 10^{-16}$  J, both of which are lower than the values of 535 and  $1.36 \times 10^{-15}$  J, respectively, when the fracture pattern is type II. In addition to the fracture pattern, the area of the fracture surface also influences the intensity of AE activity. Taking  $\theta = 30^\circ$  as an example, when the fracture pattern is type II, the AE count is 147, and the released energy is  $5.24 \times 10^{-16}$  J, which is smaller than 349 and  $9.3 \times 10^{-16}$  J, respectively, when the fracture pattern is type I, which is due to the smaller area of the fracture surface. The weaker the AE activity, the lower the failure strength; thus, failure strength is related to the fracture pattern, as indicated in Sect. 3.2.

## 5 Numerical Simulation

The particle DEM is used extensively to simulate the mechanical behavior of rock. This approach allows the entire process of the generation, propagation, and coalescence of cracks to be obtained without using a complex constitutive model. In this paper, the smooth joint model (SJM) and the flat-joint model (FJM) in the particle flow code (PFC) are combined to numerically simulate the inherent transverse isotropy of phyllite.

### 5.1 Flat-Joint Model

Before the FJM was developed, BPM was used extensively to study the properties of rocks (Potyondy and Cundall 2004; Bahaaddini et al. 2013; Yang et al. 2015a, b). However, the

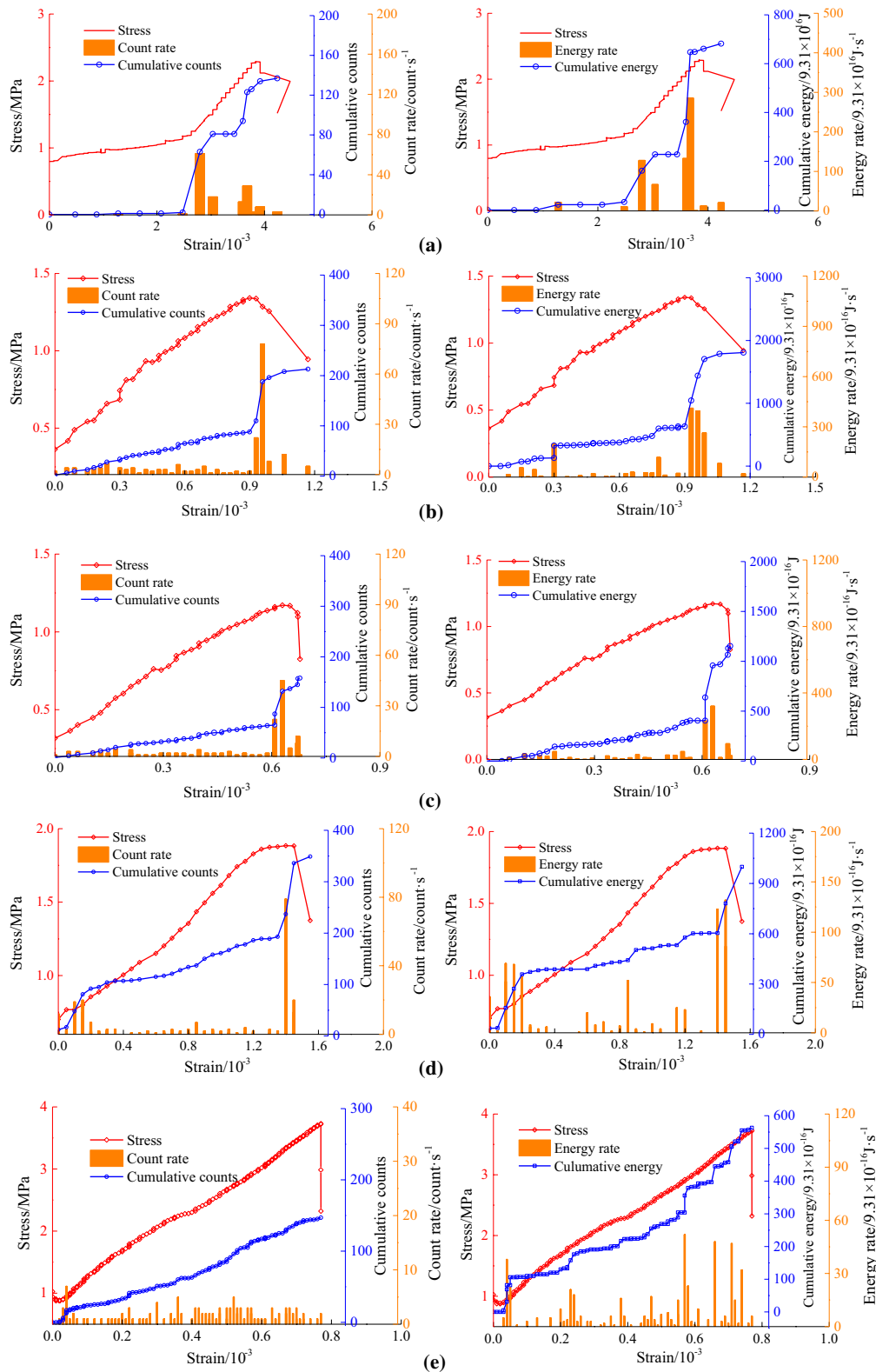


**Fig. 11** Temporal distribution of AE count and energy recorded in laboratory test. **a** N0-1 (fracture pattern of type I), **b** N15-2 (fracture pattern of type II), **c** N15-4 (fracture pattern of type I), **d** N30-1 (fracture pattern of type I), **e** N30-5 (fracture pattern of type II), **f** N45-3

(fracture pattern of type II), **g** N45-5 (fracture pattern of type I), **h** N60-2 (fracture pattern of type I), **i** N75-2 (fracture pattern of type II), **j** N75-5 (fracture pattern of type I), **k** N90-3 (fracture pattern of type II), **l** N90-4 (fracture pattern of type III)

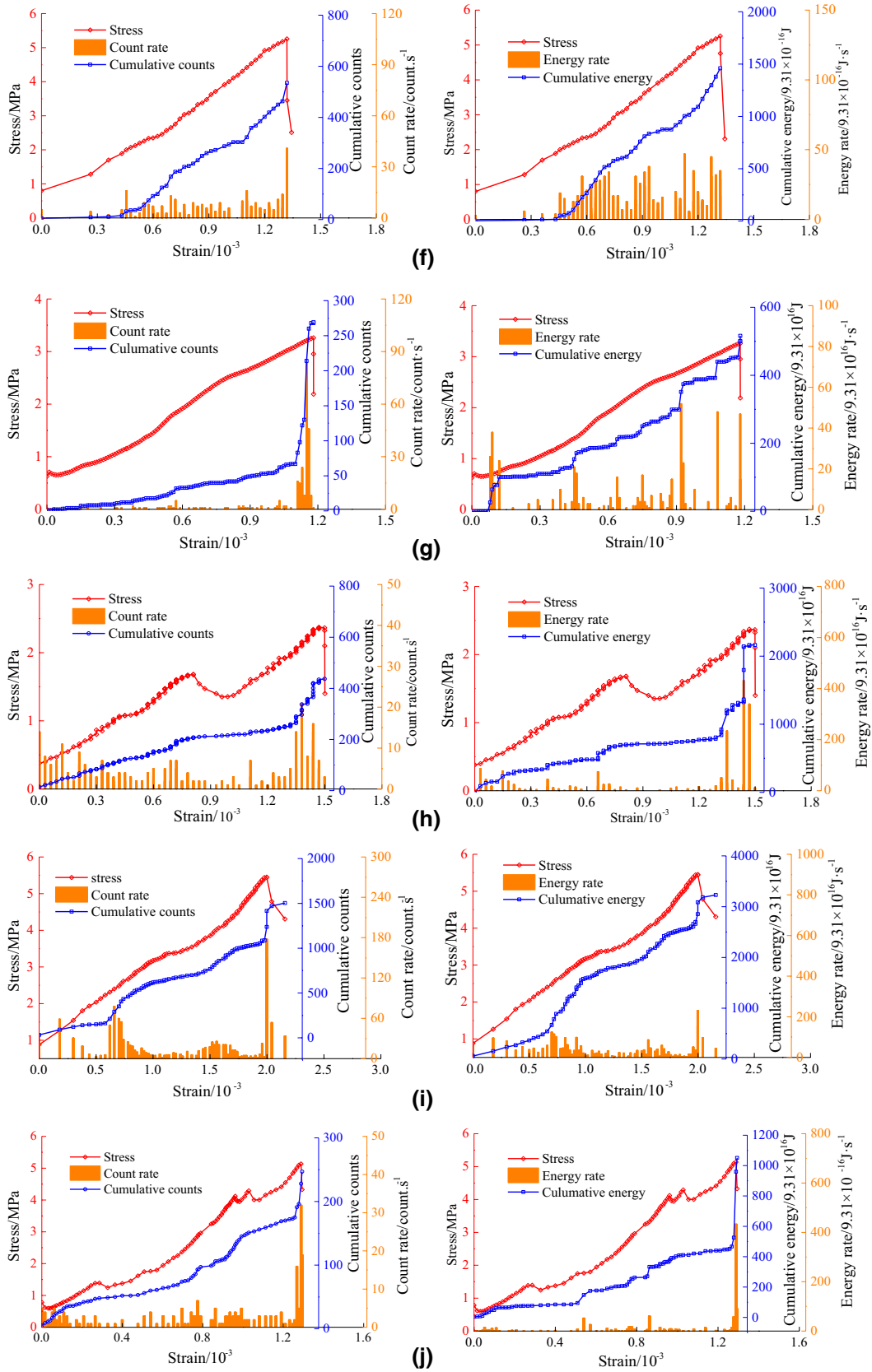


Fig. 11 (continued)



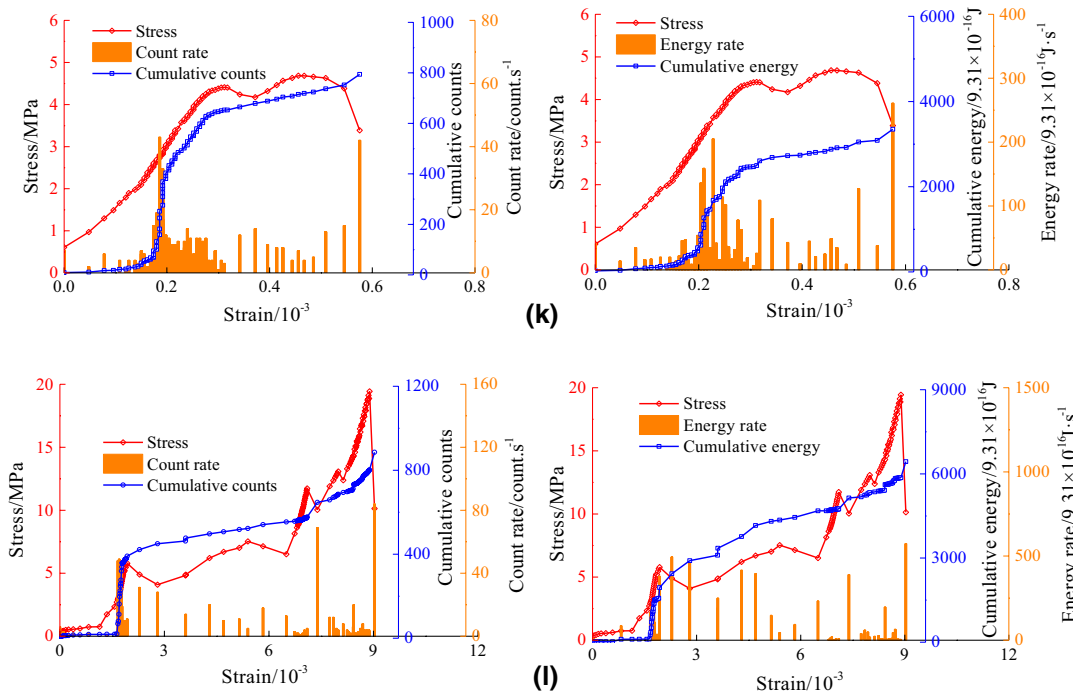


Fig. 11 (continued)

following disadvantages of BPM were found in practice: (1) Spherical particles cannot produce sufficient self-locking force; (2) when the contact surfaces of the particle ruptures, the parallel contact cannot resist the relative rotation between particles. Thus, Potyondy (2012) proposed a new contact model that was called the FJM. The detailed comparison between FJM and BPM can be found in Wu and Xu (2016). The main micro-parameters of FJM are (1) the size distribution of the particles, (2) the strength of the bond (normal strength  $\bar{\sigma}_c$  and shear strength  $\bar{\tau}_c$ ), (3) the stiffness

of the particles ( $k^n$  and  $k^s$ ), (4) the stiffness of the bond ( $\bar{k}^n$  and  $\bar{k}^s$ ), (5) the coefficient of friction between the particles ( $\mu_c$ ), (6) the installation gap ratio ( $g_{ratio}$ ), and (7) the slit element fraction ( $\varphi_s$ ).

The effect of  $g_{ratio}$  and  $\varphi_s$  on the microstructure of the rock matrix is shown in Fig. 12. A larger  $g_{ratio}$  can produce a larger coordination number (CN) value, which implies more contacts around each grain and increased grain interlocking. There are three types of flat-joint contacts. Type B (bonded contact) denotes the contact in bonded state. Type G (gapped contact) represents the contact in un-bonded state with a non-zero gap, and Type S (silted contact) denotes the contact in un-bonded state with a gap equal to zero. Type S can be used to characterize pre-existing cracks, and type G can be regarded as an open pore space in the rock. The proportion of each contact type can be adjusted by changing the value of  $\varphi_s$ . Thus, the model with a lower  $\varphi_s$  value can be envisioned as a coarse rock, whereas porous rock has a larger  $\varphi_s$  value.

Table 2 AE characteristic curves of specimens

| Foliation-loading angle | Specimen | Fracture pattern | Curves        |                |
|-------------------------|----------|------------------|---------------|----------------|
|                         |          |                  | AE event rate | AE energy rate |
| 0°                      | N0-1     | Type I           | M-I           | M-I            |
| 15°                     | N15-2    | Type II          | M-I           | M-I            |
|                         | N15-4    | Type I           | M-I           | M-I            |
| 30°                     | N30-1    | Type I           | M-I           | M-I            |
|                         | N30-5    | Type II          | M-II          | M-II           |
| 45°                     | N45-3    | Type II          | M-II          | M-II           |
|                         | N45-5    | Type I           | M-I           | M-I            |
| 60°                     | N60-2    | Type I           | M-II          | M-I            |
| 75°                     | N75-2    | Type II          | M-II          | M-II           |
|                         | N75-5    | Type I           | M-I           | M-I            |
| 90°                     | N90-3    | Type II          | M-I           | M-I            |
|                         | N90-4    | Type III         | M-I           | M-I            |

### 5.2 Smooth Joint Model

The SJM is used extensively to simulate the mechanical behavior of a joint (Huang et al. 2015; Vallejos et al. 2016). When the SJM is used in a numerical model, the original contacts among particles located near joint planes are replaced, and these particles with the SJM can slide along joint planes rather than move around one another.

Equation 3 can be used to derive the micro-parameters of the SJM from the micro-parameters of the FJM:

**Fig. 12** Effect of  $g_{ratio}$  and  $\varphi_S$  on the microstructure of the rock matrix: **a**  $g_{ratio} = 0.5, \varphi_S = 0$ ; **b**  $g_{ratio} = 0, \varphi_S = 0$ ; **c**  $g_{ratio} = 0.3, \varphi_S = 0.1$ ; **d**  $g_{ratio} = 0.3, \varphi_S = 0.5$

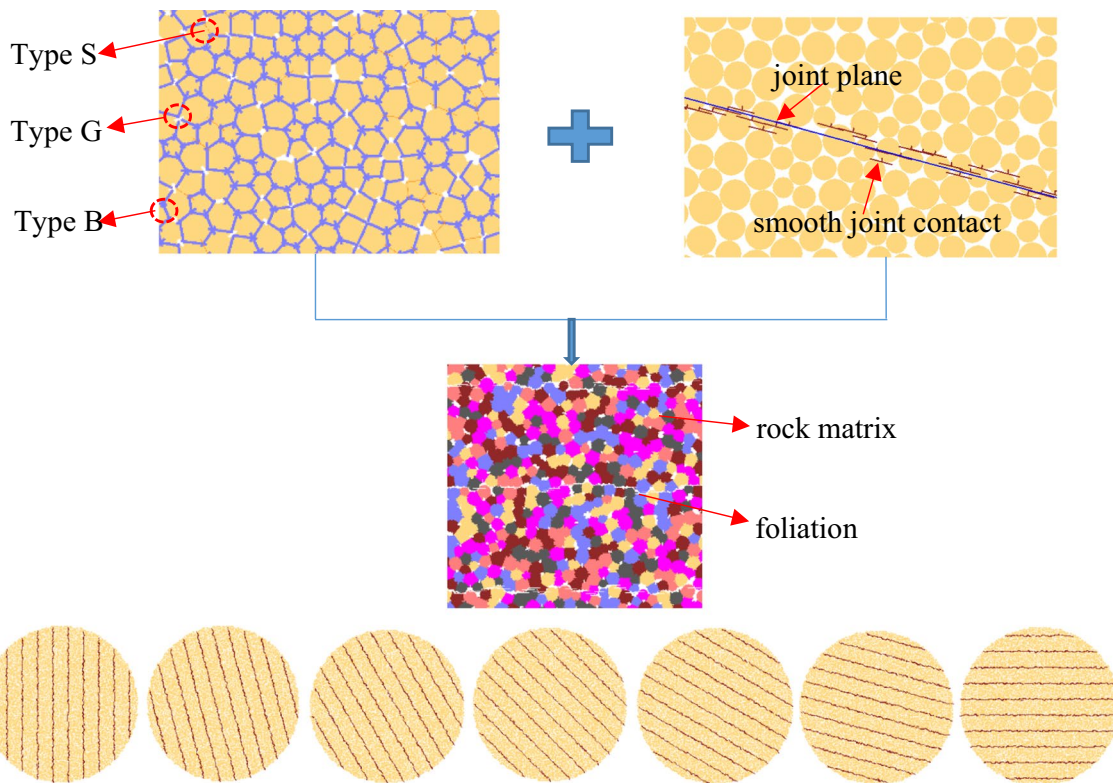
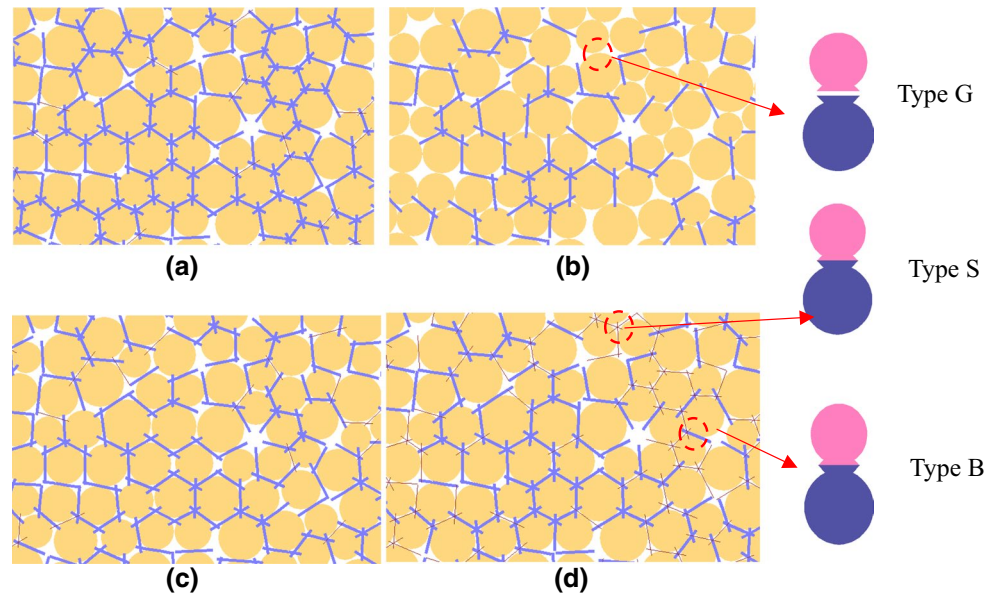


**Fig. 13** Generation of specimens

$$\begin{cases} \bar{\lambda} = \bar{\lambda}_{pb} \\ \bar{k}_n = (k^n/A) + \bar{k}^n \\ \bar{k}_s = (k^s/A) + \bar{k}^s \\ \mu = \mu_c \\ \sigma_c = \bar{\sigma}_c \\ c_b = \bar{c}_c \\ \varphi_b = 0 \end{cases}, \tag{3}$$

where  $\bar{k}_n$  and  $\bar{k}_s$  are the normal and shear stiffness, respectively,  $\bar{\lambda}$  is the radius multiplier,  $\mu$  is the friction coefficient,  $\sigma_c$  and  $c_b$  are the normal strength and cohesion, respectively, and  $\varphi_b$  is the friction angle between particles.

### 5.3 Generation of a Specimen

As shown in Fig. 13, the generation of a transversely isotropic specimen requires two steps:

1. Generating an isotropic Brazilian disk. The smallest diameter of the particles is 0.2 mm, and the ratio of the maximum diameter to the minimum diameter is 1.66. The percentage of cracks that existed prior to testing accounted for 10% of the total number of contacts, and all contacts between particles are modeled by the FJM.
2. Applying the SJM to the isotropic Brazilian disk. The space between foliations is 5 mm. This distance ensures that the specimen with an adequate foliation number will represent the transverse isotropy of the rock at the macro-level.

### 5.4 Calibration and Simulation

In the DEM model, the micro-parameters were calibrated based on the experimental results. The steps in the calibration procedure are as follows:

1. Determine deformation parameters of the DEM model through uniaxial compression test results.
  - (a) When  $\theta = 0^\circ$ , the stiffness of foliation has the least influence on the Young's modulus of the specimen. The stiffness of the FJM ( $k^n, k^s, \bar{k}^n, \bar{k}^s$ ) is calibrated to match the  $E_0$  (Young's modulus for  $\theta = 0^\circ$ ) obtained from laboratory testing.
  - (b) The stiffness of the SJM ( $\bar{k}_n, \bar{k}_s$ ) is calibrated to match the  $E_{90}$  (Young's modulus for  $\theta = 90^\circ$ ) obtained from laboratory testing;  $\bar{k}_n$  and  $\bar{k}_s$  are set equal to reduce the number of free parameters.
2. Determine the strength parameters of the DEM model using the Brazilian test results.
  - (a) When  $\theta = 90^\circ$ , the strength of foliation has the least influence on the strength of the specimen.

**Table 3** Micro-parameters of FJM

| Particle properties          | Value | Bond properties        | Value      |
|------------------------------|-------|------------------------|------------|
| $E_c$ (GPa)                  | 30    | $\bar{E}_c$ (GPa)      | 30         |
| $k^n/k^s$                    | 2.5   | $\bar{k}^n/\bar{k}^s$  | 2.5        |
| $\mu$                        | 0.5   | $\bar{\sigma}_c$ (MPa) | $40 \pm 7$ |
| $R_{max}/R_{min}$            | 1.66  | $\bar{\tau}_c$ (MPa)   | $40 \pm 7$ |
| $R_{min}$ (mm)               | 2.2   | $g_{ratio}$            | 0.3        |
| $\rho$ (kg m <sup>-3</sup> ) | 2800  | $\varphi_s$            | 0.1        |
|                              |       | $\varphi_r$ (°)        | 5          |

Thus, the strength of the FJM ( $\bar{\sigma}_c, \bar{\tau}_c$ ) is calibrated to reproduce the value of  $\sigma_{90}$  obtained from the laboratory test.

- (b) Based on the trends in the variation of the failure strength with the foliation-loading angle, the strength parameters of the SJM ( $\sigma_c, c_b, \varphi_b$ ) are calibrated.

The DEM model is calibrated using the above procedure to reproduce the behaviors of the phyllite specimen during the Brazilian test. The micro-parameters of the FJM and SJM are shown in Tables 3 and 4, respectively.

Good agreement in the values of failure strength was found between the numerical and experimental results (Fig. 14). When  $\theta$  varied from  $0^\circ$  to  $60^\circ$ , there were small changes in the amplitude of the failure strength. Then, the changes increased in amplitude as the value of  $\theta$  increased.

Figure 15 shows a typical fracture pattern of specimens observed during numerical simulation and laboratory tests. When  $\theta$  varied from  $0^\circ$  to  $60^\circ$ , the specimens failed along the foliation. For  $\theta = 0^\circ$ , both shear and tensile failure occurred. For  $\theta$  values in the range of  $15^\circ$ – $60^\circ$ , only shear failure occurred. When  $\theta$  varied from  $75^\circ$  to  $90^\circ$ , fracture occurred along and across the foliation. In this condition, damage in the rock matrix was caused by tensile and shear failure, while damage along the foliation was produced by shear failure.

**Table 4** Micro-parameters of SMJ

| Parameter  | Value |
|--|-------|
| Normal stiffness, $\bar{k}_n$ (GPa m <sup>-1</sup> ) | 6000  |
| Shear stiffness, $\bar{k}_s$ (GPa m <sup>-1</sup> )  | 6000  |
| Friction coefficient, $\mu$                          | 0.5   |
| Dilation angle, $\psi$                               | 0     |
| Tensile strength, $\sigma_c$ (MPa)                   | 6     |
| Cohesion, $\tau_c$ (MPa)                             | 6     |
| Friction angle, $\varphi_b$ (°)                      | 0     |

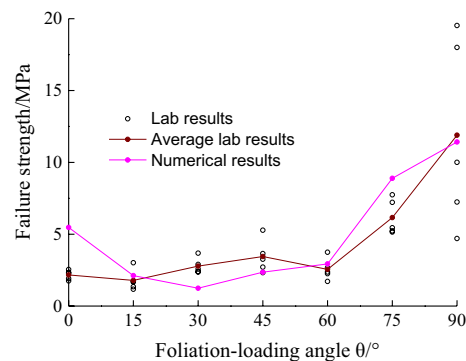


**Fig. 14** Failure strength of numerical simulation in comparison with laboratory tests



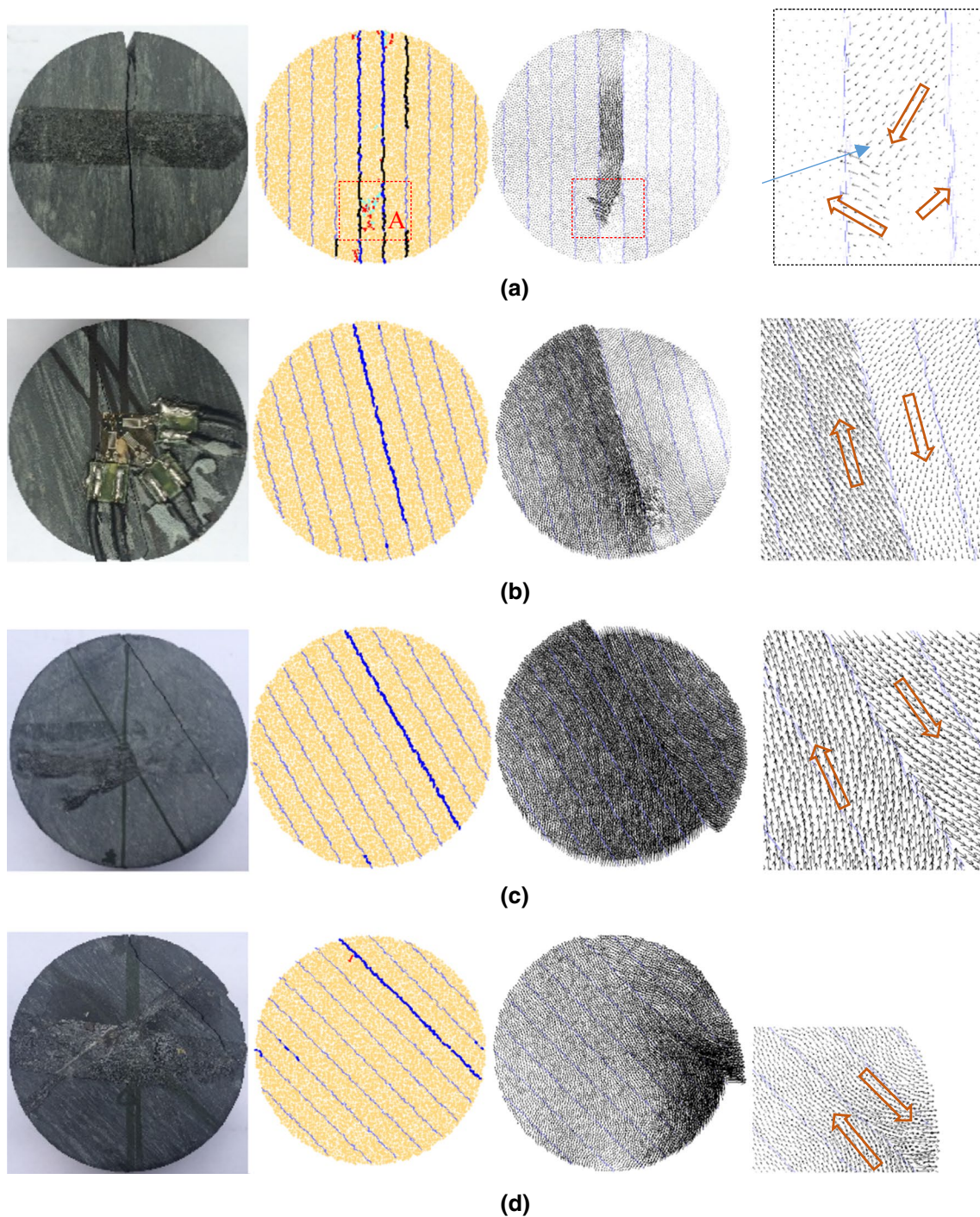


**Fig. 15** Fracture patterns for different foliation-loading angles: **a**  $\theta = 0^\circ$ ; **b**  $\theta = 15^\circ$ ; **c**  $\theta = 30^\circ$ ; **d**  $\theta = 45^\circ$ ; **e**  $\theta = 60^\circ$ ; **f**  $\theta = 75^\circ$ ; **g**  $\theta = 90^\circ$ . First column the fracture patterns observed in the laboratory test; Second column the results of numerical simulation (black segment denotes tensile failure of smooth joint contacts, navy blue segment denotes shear failure of smooth joint contacts, red seg-

ment denotes tensile failure of flat-joint contacts, light cyan segment denotes shear failure of flat-joint contacts); Third column velocity field (arrow size represents the magnitude of the velocity); Fourth column partial enlarged detail (orange arrow denotes motion direction of particles) (color figure online)

The direction of the movement of particles on opposite sides of the fracture surface was related closely to the fracture pattern. For  $\theta = 0^\circ$ , the velocity of rock particles

between two macro-cracks was much greater than that of the outside part. At the coalescence part of the two macro-cracks (Part A in Fig. 15a), the motion field appears to be



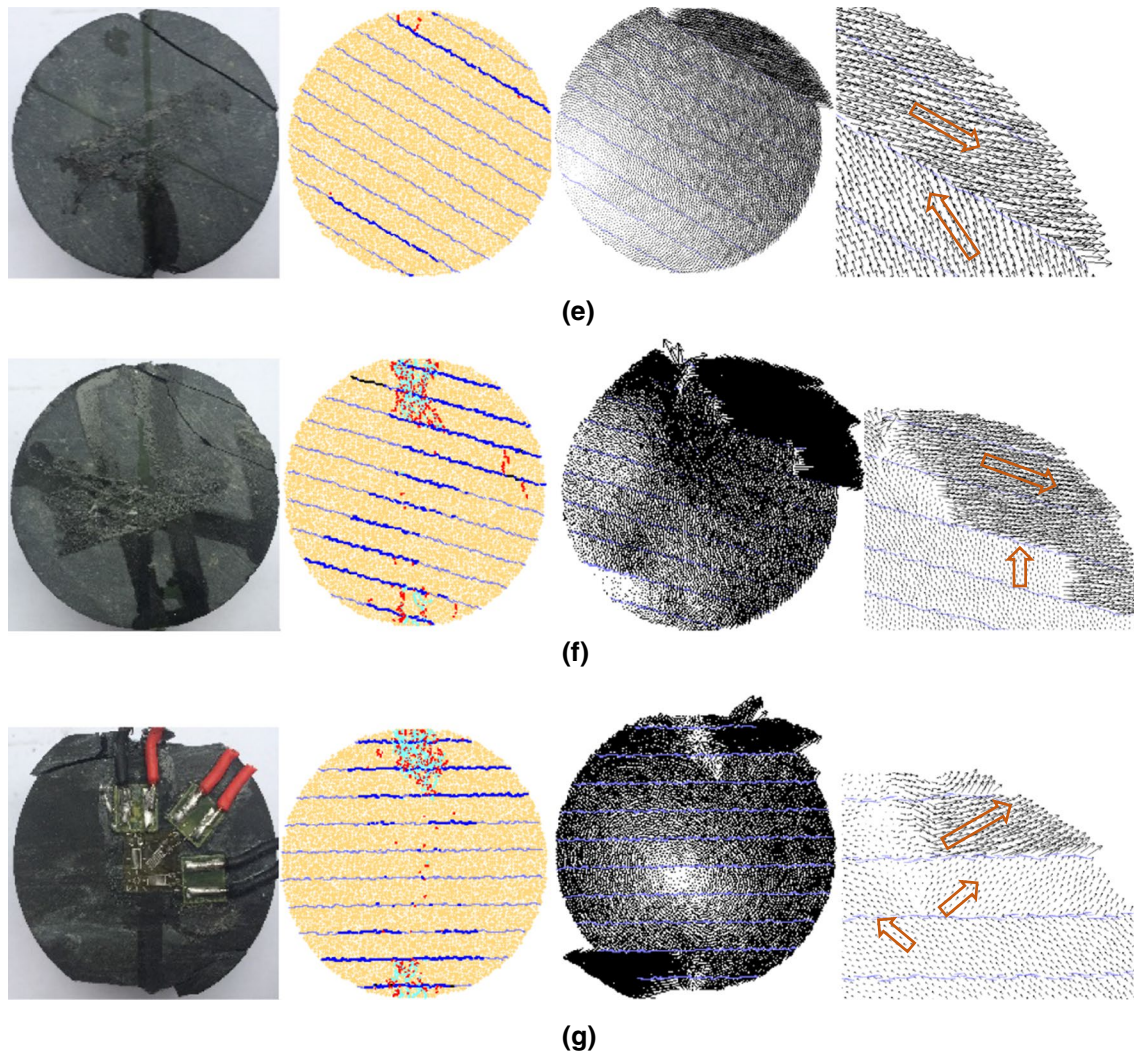


Fig. 15 (continued)

bifurcated, forming an inverted arrow. For  $\theta$  values in the range of  $15^\circ$ – $60^\circ$ , the particles on opposite sides of the shear crack moved in opposite directions parallel to the fracture surface. For  $\theta = 75^\circ$ , particles outside the fracture surface moved outward in the direction parallel to foliation, while the inner particles moved parallel to the axial loading direction. For  $\theta = 90^\circ$ , particles outside the fracture surface moved outward in a direction that was approximately parallel to foliation, while the motion field of the inner particles appeared to be bifurcated at the coalescence area of the cracks.

Figure 16 shows the relationship between the AE count and the strain. Figure 17 shows the failure process of the specimen. In the DEM model, the generation of a new micro-crack represented the generation of an AE count.

For  $\theta = 0^\circ$  (Fig. 16a), the relationship between the AE count and the strain belonged to M-II. At the initial loading stage (point a), shear cracks appeared near the upper

loading position. Then, the shear cracks propagated along the foliation (point b) with their number rising sharply (point c). Tensile cracks occurred at the tip of the shear cracks and propagated along the foliation. The number of cracks showed a uniform growth trend from point a to point c. After the specimen was loaded to point d, with the load transform, tensile and shear cracks began to appear in the rock matrix. At the end of the loading process, a small crushing area appeared at the upper loading position, and the coalescence of the two macro-cracks occurred near the lower loading position.

For  $\theta$  values in the range of  $15^\circ$ – $60^\circ$ , the relationship of the AE event with strain belonged to M-I. When  $\theta = 15^\circ$  or  $30^\circ$ , cracks appeared until the specimens were loaded to near the peak strength. When  $\theta = 45^\circ$  or  $60^\circ$ , the AE count was more dispersed during the loading process. The fracture patterns of different  $\theta$  values were similar. The failure process was described by taking  $\theta = 45^\circ$  as

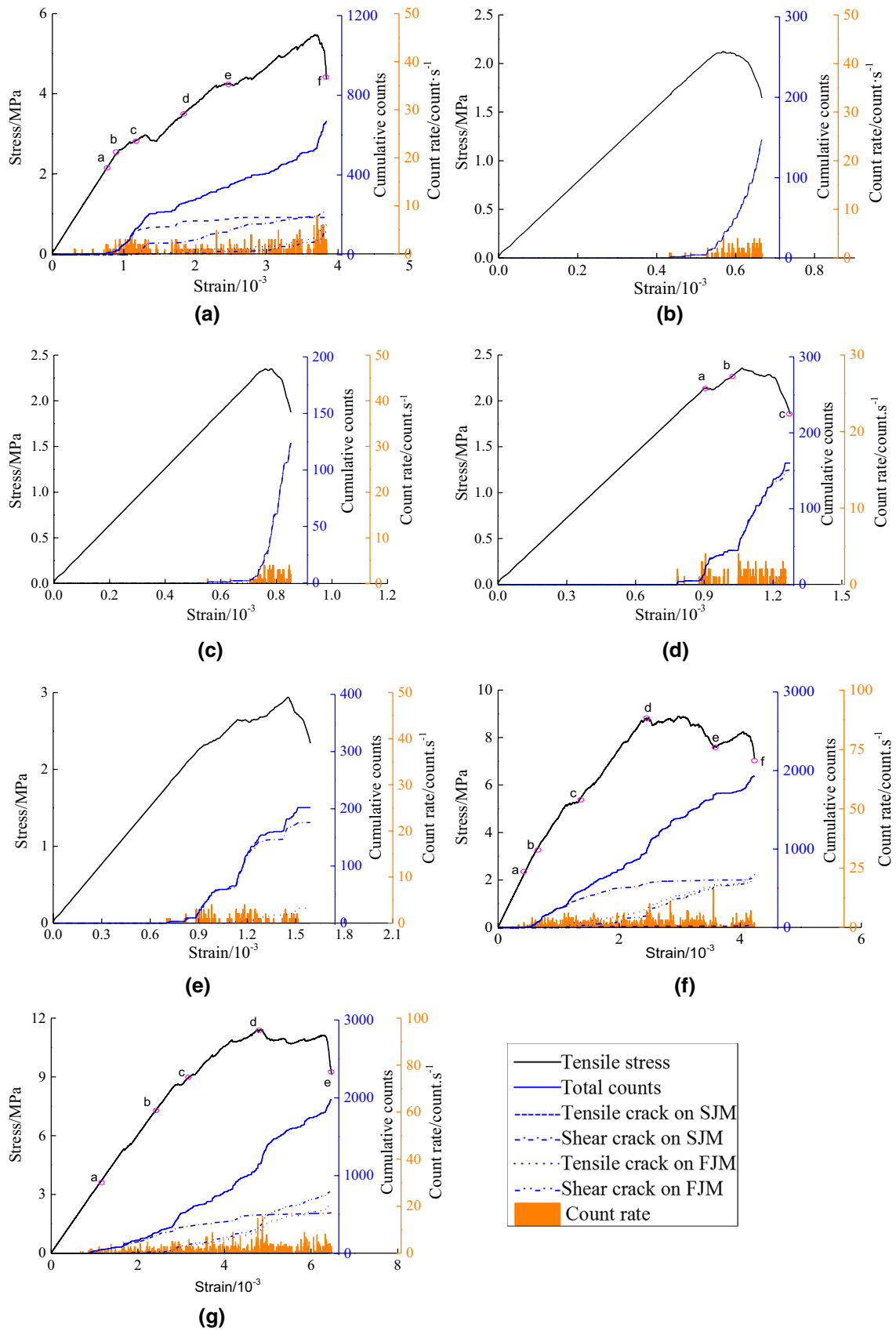
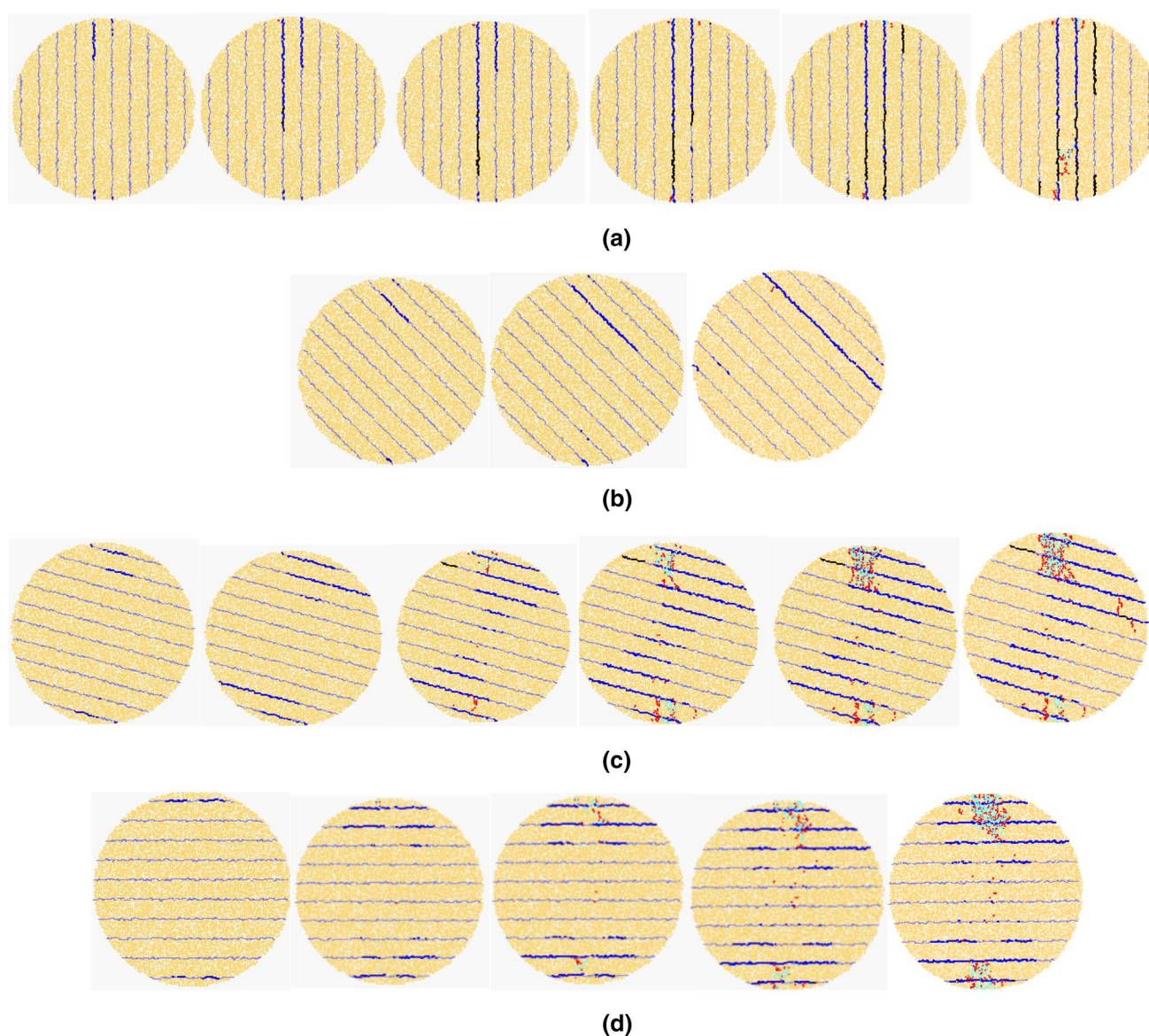


Fig. 16 Temporal distribution of AE counts: a  $\theta = 0^\circ$ ; b  $\theta = 15^\circ$ ; c  $\theta = 30^\circ$ ; d  $\theta = 45^\circ$ ; e  $\theta = 60^\circ$ ; f  $\theta = 75^\circ$ ; g  $\theta = 90^\circ$





**Fig. 17** Fracture process: **a**  $\theta = 0^\circ$ ; **b**  $\theta = 45^\circ$ ; **c**  $\theta = 75^\circ$ ; **d**  $\theta = 90^\circ$ . (Corresponding to points “a”, “b”, “c”, etc. in Fig. 15 for each foliation-loading angle from left to right)

an example. First, cracks appeared near the upper loading position because of the concentrated shear stress. Then, these cracks propagated along the foliation. Finally, a macro-crack was formed throughout the foliation. During the loading process, the three other kinds of cracks did not appear, except for the shear cracks of the SJM. The shear strength of the foliation was lower than that of the rock matrix; thus, shear failure along the foliation occurred before the tensile strength of the rock matrix was reached.

For  $\theta$  values in the range of  $75^\circ$ – $90^\circ$ , the relationship of the AE count with strain belonged to M-II, and the failure process was relatively complex. Taking  $\theta = 90^\circ$  for example, cracks appeared at the foliation nearest the loading

position (point a) and near the loading position (point b). During this period, the three other types of cracks do not appear, except for the shear cracks of the SJM. With increasing axial load, tensile cracks and shear cracks appeared in the rock matrix due to the relative movement between the foliations. The aforementioned steps were repeated until the specimen broke.

The above description indicated that the DEM model was superior in reflecting the failure mechanism of the rock at the mesoscopic level. However, the curves of the AE count that were obtained from the numerical simulation and the experimental results for  $\theta = 0^\circ$  were not the same because the specimen split along the two foliations in the numerical

approach, causing a gradual failure process. However, in the laboratory test, the specimen split only along the central foliation, resulting in an abrupt failure process.

## 5.5 Sensitivity Analysis

A systematic analysis was conducted to investigate the influence of the strength of foliation and the microstructure of the rock matrix on the failure strength and fracture patterns of the specimens. In the DEM model, the micro-cracks underwent shear and tensile failure on the flat-joint contacts and the smooth joint contacts. The percentage of each crack was displayed through normalization by the total number of micro-cracks. The cases of sensitivity analysis were as follows:

1. Effects of CN:  $\sigma_c = \tau_c = 20$  MPa,  $\varphi_S = 0.1$ ,  $g_{\text{ratio}} = 0, 0.15, 0.3, 0.5$ .
2. Effect of pre-existing cracks:  $\sigma_c = \tau_c = 20$  MPa,  $g_{\text{ratio}} = 0.3$ ,  $\varphi_S = 0, 0.1, 0.3, 0.5$ .
3. Effects of smooth joint strength:  $\varphi_S = 0.1$ ,  $g_{\text{ratio}} = 0.3$ ,  $\sigma_c = \tau_c = 6, 10, 20$ , and 40 MPa.
4. Effects of the ratio of cohesion strength to tensile strength:  $\varphi_S = 0.1$ ,  $g_{\text{ratio}} = 0.3$ ,  $\sigma_c = 6$  MPa,  $\tau_c = 6, 10, 20$ , and 40 MPa.

Other micro-parameters are the same as the parameters shown in Tables 3 and 4.

### 5.5.1 Effects of CN

As illustrated in Fig. 18b, the curve of failure strength was similar to trend I for a loose rock ( $g_{\text{ratio}} = 0$  in this case), which shows the feature of isotropic rocks. However, the strength curve was trend IV in the other cases. For each angle, the failure strength increased as the  $g_{\text{ratio}}$  increased. When the factor reached a certain high value (0.3 in this case), further increases in the  $g_{\text{ratio}}$  did not increase the failure strength any further. In each case, tensile cracks on the FJM were dominant (Fig. 18b). The increase in  $g_{\text{ratio}}$  caused an increasing percentage of shear cracks on the SJM, indicating that the effect of foliation begins to appear for rocks with a fine compact rock matrix.

### 5.5.2 Effects of Pre-existing Cracks

Figure 19b shows that the value of  $\varphi_S$  had a strong influence on the trends of failure strength. The variation of strength changed from trend IV ( $\varphi_S = 0, 0.1$ ) to trend I ( $\varphi_S = 0.3, 0.5$ ). The percentage of cracks generated on the SJM decreased as  $\varphi_S$  increased. Considering the fracture pattern,

when  $\varphi_S$  reached a high value ( $\varphi_S = 0.3, 0.5$ ), the fracture planes were dominated by tensile cracks that propagated along the loading direction. This phenomenon indicated that the effect of foliation on failure strength and the fracture pattern was negligible for rocks with well-developed cleavage in rock matrix.

### 5.5.3 Effects of Smooth Joint Strength

As shown in Fig. 20b, the specimen presented isotropic characteristics when the strength of the SJM was equal to the strength of the rock matrix; thus, the failure strength remained almost constant over the entire interval (trend I). When the strength of the SJM decreased, increases in  $\theta$  from  $0^\circ$  to  $15^\circ$  resulted in a reduction in the failure strength, but the strength remained constant between  $15^\circ$  and  $45^\circ$ , after which an approximately linear increase occurred.

When the strength of the smooth joint was reduced by a factor of 1/8 or 1/4, cracks that occurred at the low foliation-loading angles ( $15^\circ$ – $60^\circ$ ) were predominantly shear cracks on the SJM, and the fracture plane occurred along the foliation. When the ratio was larger (1/2), cracks at all angles were predominantly tensile cracks on the FJM, and the percentage of cracks on the SJM decreased to less than 20%. When the strength of SJM was identical to the strength of the FJM, the cracks were produced almost entirely on the flat-joint contacts, and the fracture planes were roughly parallel to the loading direction and located in the central part of the disk specimens.

### 5.5.4 Effects of the Tensile Strength-to-Cohesion Ratio

As shown in Fig. 21b, when the shear strength of the SJM was equal to that of the FJM, the failure strength increased for the low foliation-loading angles ( $0^\circ$ – $30^\circ$ ) and then leveled off. The strength curve was consistent with trend II. When the shear strength of the SJM was reduced by a factor of 1/2, the failure strength remained constant between the angles of  $15^\circ$  and  $60^\circ$ , after which there was a linear increase. The strength curve was consistent with trend IV. The failure strength decreased with a further reduction in the shear strength of the SJM, but the trend of the strength curve continued to follow trend IV.

The ratio of tensile strength to cohesion exhibited a significant influence on the cracks produced at various contacts. For each ratio, the percentage of cracks initiated from the SJM decreased as the foliation-loading angle increased. For each angle, the percentage of cracks initiated from the SJM decreased as the ratio decreased. Taking  $\theta = 45^\circ$  as an example, when the ratio was 3/5, shear cracks on the SJM were dominant, and the failure plane was aligned primarily along the foliation. With a decrease in the ratio to 3/10, the tensile cracks on the FJM dominated, and the failure plane was

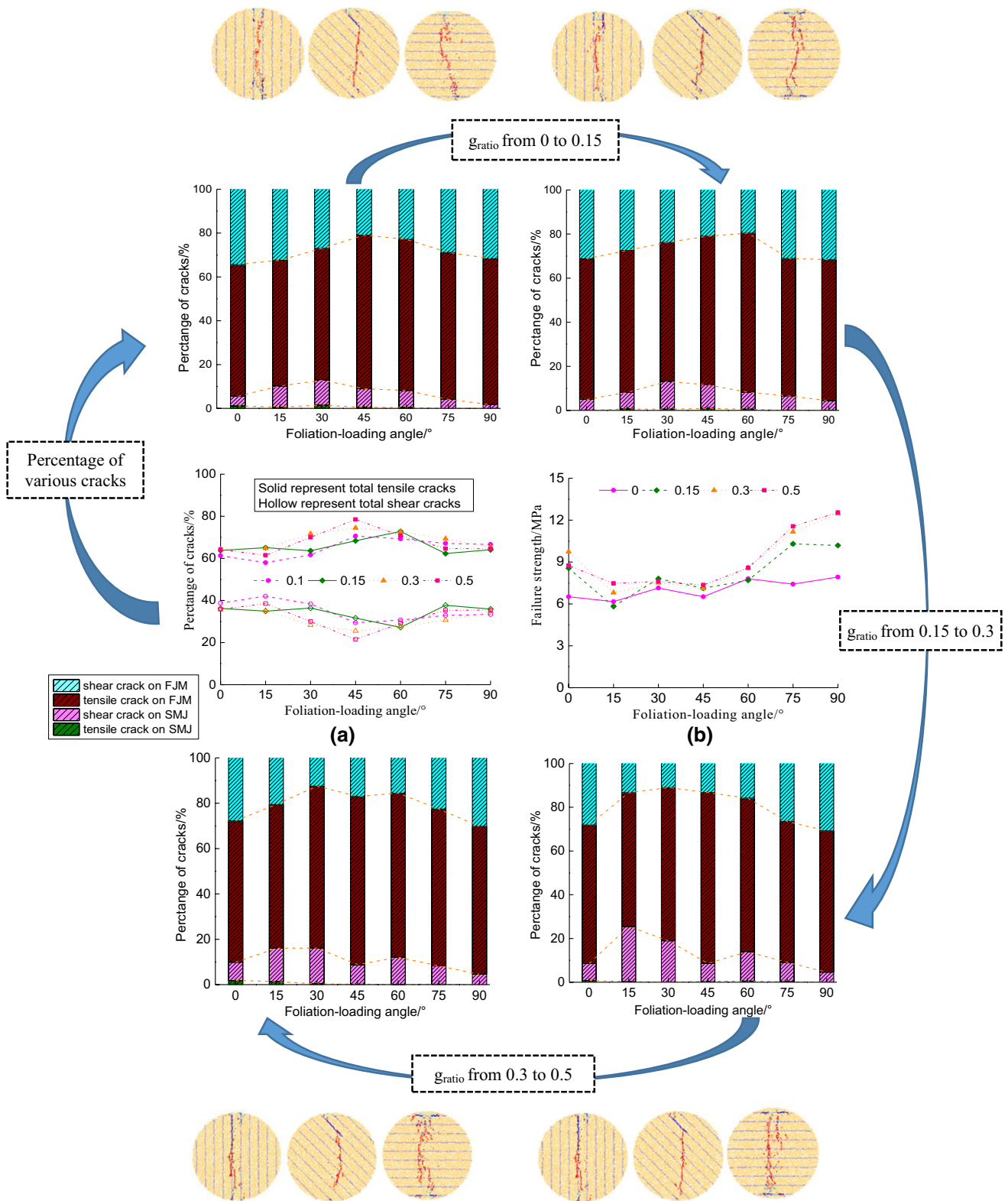


Fig. 18 Effects of CN: **a** percentage of cracks; **b** failure strength



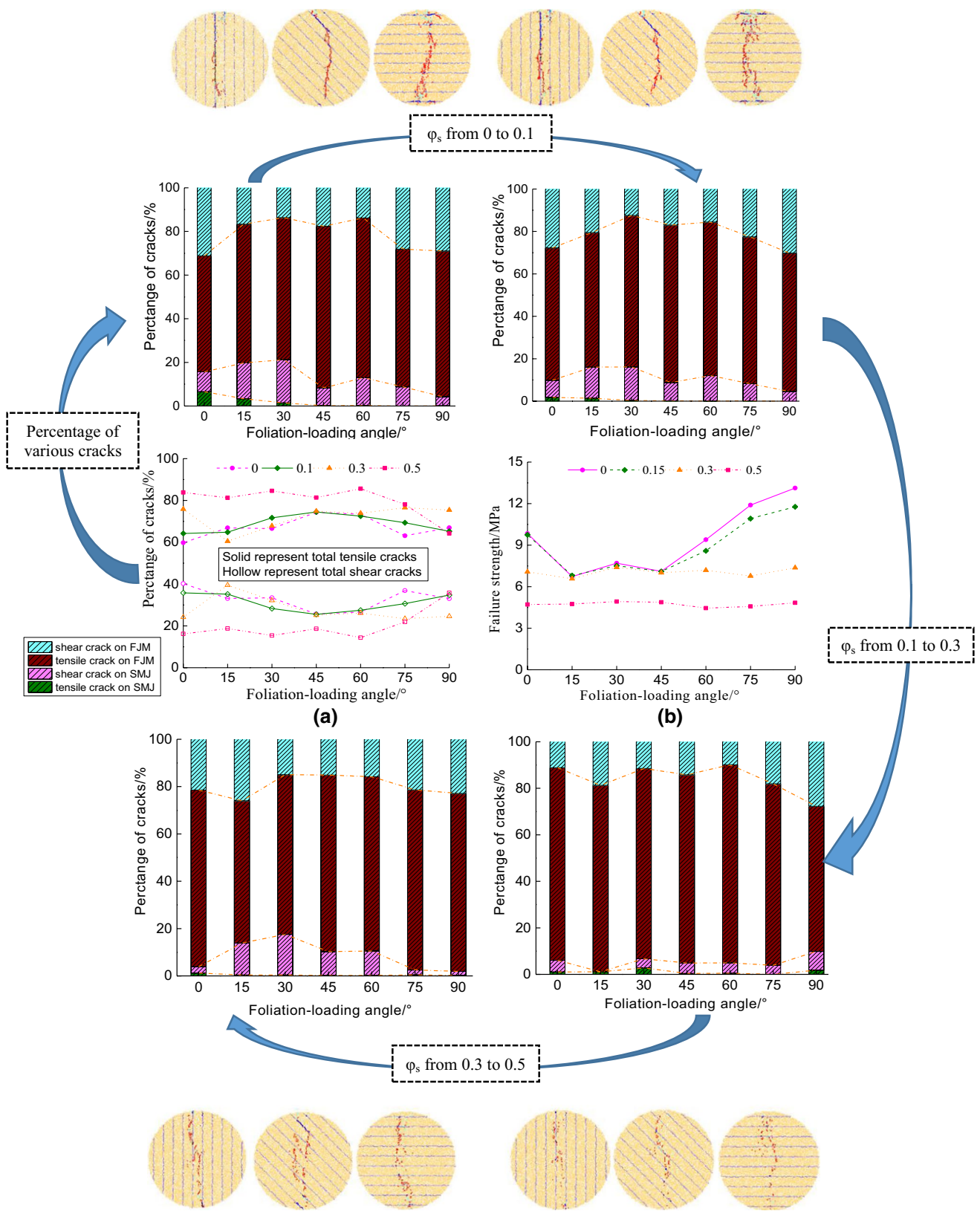


Fig. 19 Effects of pre-existing cracks: **a** percentage of cracks; **b** failure strength

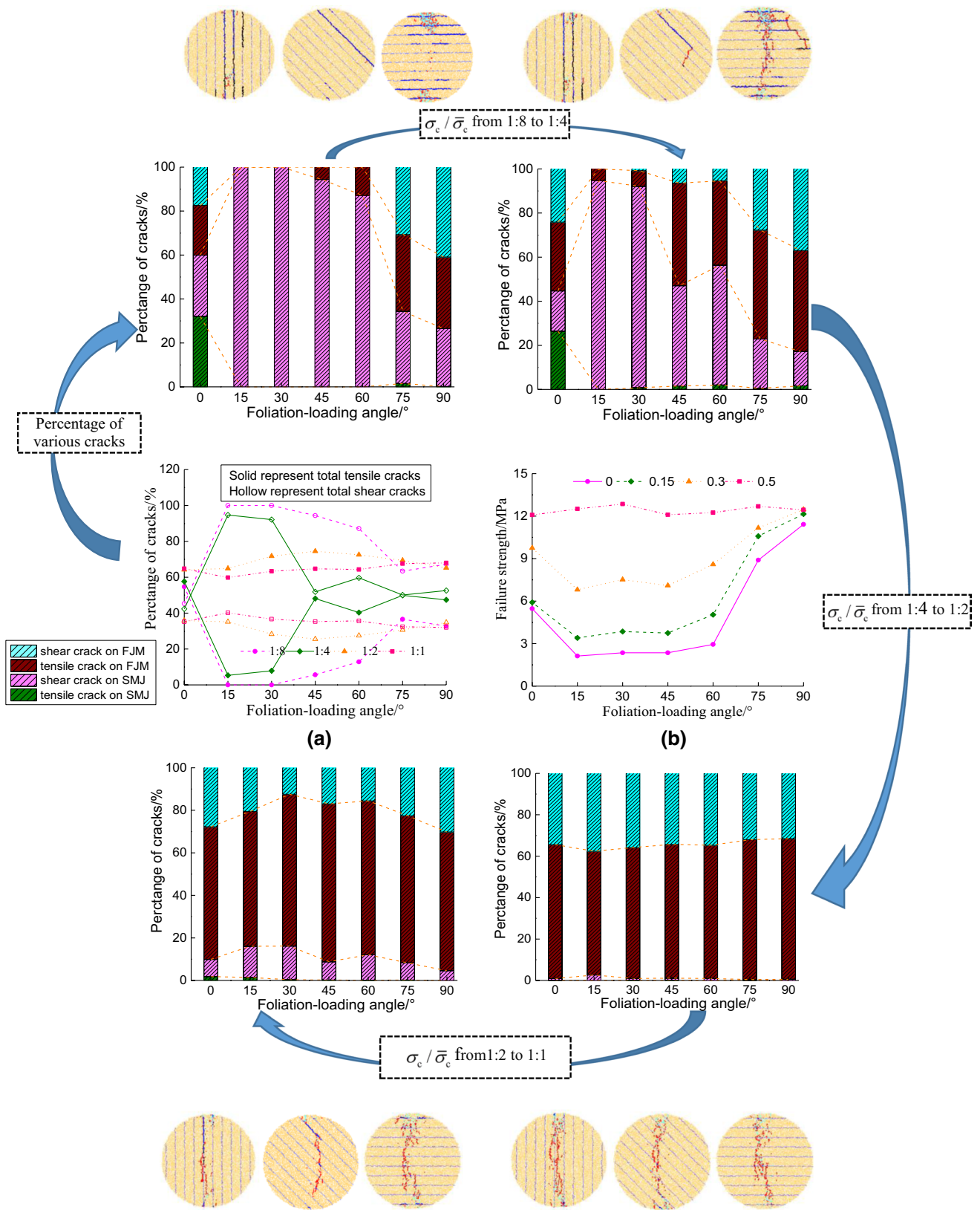
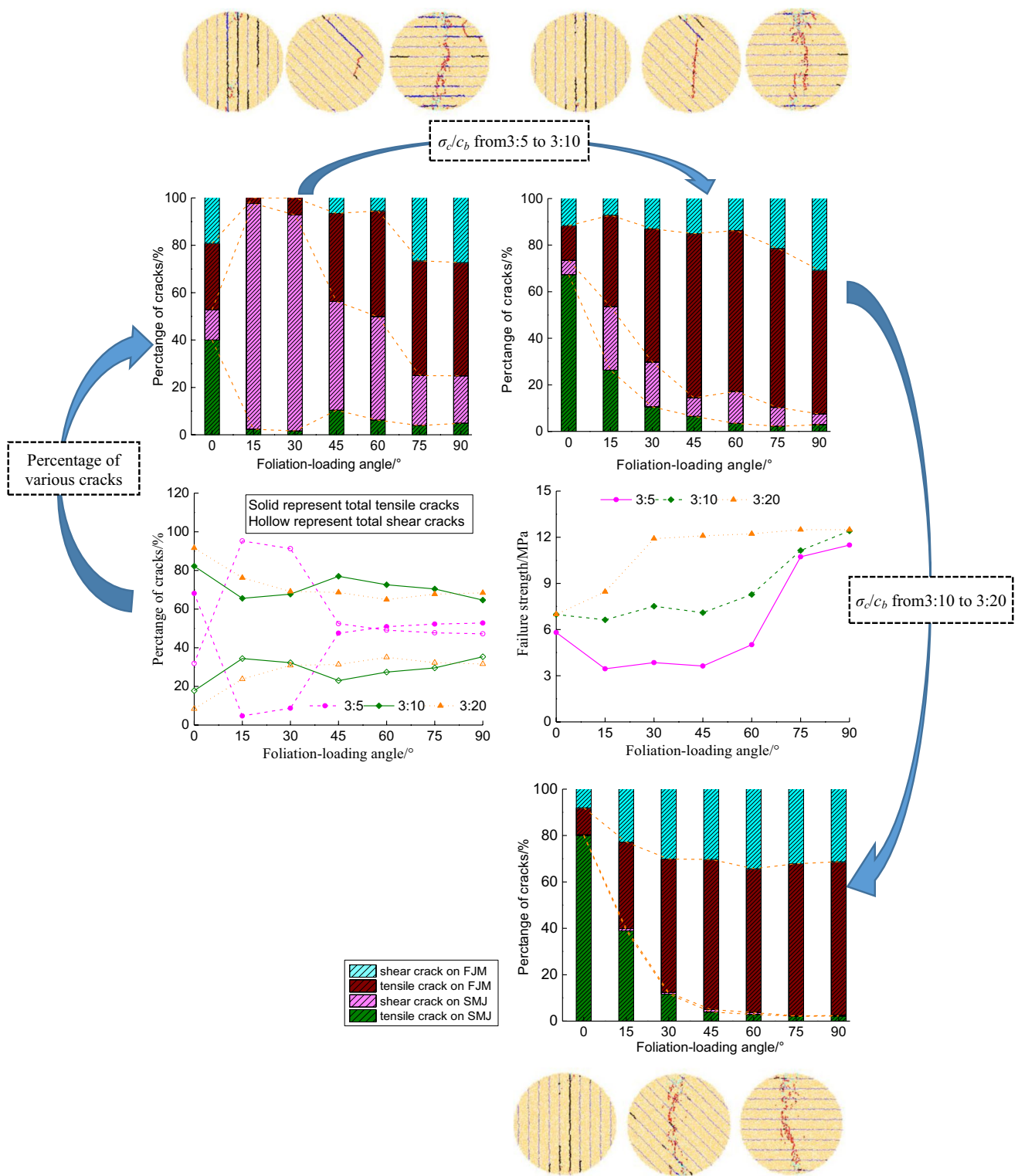


Fig. 20 Effects of smooth joint strength: a percentage of cracks; b failure strength



**Fig. 21** Effects of the ratio of cohesion to tensile strength of smooth joint: **a** percentage of cracks; **b** failure strength

aligned primarily across the foliation. When the ratio was sufficiently low, the cracks produced were almost entirely on the flat-joint contacts, and the failure plane was a central plane that was parallel to the loading direction.

### 6 Conclusions

Brazilian tests were performed to study the fracture mechanisms of phyllite. High-speed photography and the AE test



method were used to investigate the processes of the initiation and propagation of cracks. A new DEM approach was proposed to systematically examine the mechanical behavior of transversely isotropic rock. The main conclusions of this study are as follows:

1. The maximum failure strength of phyllite occurs when the foliation-loading angle,  $\theta$ , is equal to  $90^\circ$ ; the strength then decreases sharply as the value of  $\theta$  decreases, but it remains constant as the values of  $\theta$  are decreased from  $60^\circ$  to  $0^\circ$ . The failure strengths of the specimens at the same values of  $\theta$  were scattered, and the strength values were related to the fracture pattern and the area of the fracture surface.
2. The initial cracking point of the specimens appeared at the upper or lower loading positions; the cracks propagated to the boundaries of specimens along or across the foliation. The types of AE count rate and energy rate for different values of  $\theta$  during the loading period can be divided into two modes: M-I, which is the peak mode (the distribution of the AE count rate presents 1, 2 or finite peak intervals), and M-II, which is the uniformly distributed mode, i.e., the distribution of the AE rate is uniform. When the failure pattern is layer activation, the AE characteristic curves always present a unimodal or a bimodal distribution, indicating that the rock is prone to brittle failure in this condition. When the failure patterns of the specimens were non-layer activation or mixed failure, the AE characteristic curves always presented a multimodal or uniform distribution, indicating that the rock is prone to plastic failure in this condition.
3. Strong agreement was observed between the numerical and experimental results in terms of failure strength and the failure process. As the pre-existing crack density increased or the coordination number decreased, the effect of the foliation was negligible, and the numerical simulation results indicated isotropy. In addition, the strength of foliation or the ratio of the cohesion strength to the tensile strength of foliation mainly affected the percentages of the different kinds of cracks that were formed, thereby affecting the failure strength and failure patterns of rocks.

**Acknowledgements** This research was supported by the National key research and development program of China (Grant No. 2016YFC0802201).

### Compliance with ethical standards

**Conflict of interest** The authors declare that they have no conflict of interest.

## References

- Amadei B, Rogers JD, Goodman RE (1983) Elastic constants and tensile strength of anisotropic rocks. In: Proceedings of the 5th international congress on rock mechanics, Melbourne, Australia
- Bahaaddini M, Sharrock G, Hebblewhite BK (2013) Numerical investigation of the effect of joint geometrical parameters on the mechanical properties of a non-persistent jointed rock mass under uniaxial compression. *Comput Geotech* 49:206–225
- Barla G, Innaurato N (1973) Indirect tensile testing of anisotropic rocks. *Rock Mech* 5:215–230
- Blümling P, Bernier F, Lebon P, Martin CD (2007) The excavation damaged zone in clay formations: time-dependent behavior and influence on performance assessment. *Phys Chem Earth* 32:588–599
- Chen CS, Pan E, Amadei B (1998) Determination of deformability and tensile strength of anisotropic rock using Brazilian tests. *Int J Rock Mech Min Sci* 35:43–61
- Cho JW, Kim H, Jeon S, Min KB (2012) Deformation and strength anisotropy of Asan gneiss, Boryeong shale, and Yeoncheon schist. *Int J Rock Mech Min Sci* 50:158–169
- Dan DQ (2011) Brazilian test on anisotropic rocks-laboratory experiment, numerical simulation and interpretation. Dissertation, TU Bergakademie Freiberg
- Debecker B (2009) Influence of planar heterogeneities on the fracture behavior of rock. Dissertation, University of Leuven
- Duan K, Kwok CY (2015) Discrete element modeling of anisotropic rock under Brazilian test conditions. *Int J Rock Mech Min Sci* 78:46–56
- Huang D, Wang JF, Liu S (2015) A comprehensive study on the smooth joint model in DEM simulation of jointed rock masses. *Granul Matter* 17:775–791
- Khanlari GR, Heidari M, Sepahigero AA, Fereidooni D (2014) Quantification of strength anisotropy of metamorphic rocks of the Hamedan province, Iran, as determined from cylindrical punch, point load and Brazilian tests. *Eng Geol* 169:80–90
- Kim H, Cho JW, Song I, Min KB (2012) Anisotropy of elastic moduli, P-wave velocities, and thermal conductivities of Asan Gneiss, Boryeong Shale, and Yeoncheon Schist in Korea. *Eng Geol* 147:68–77
- Lekhnitskii SG (1968) *Anisotropic plates*. Gordon and Breach, New York
- Lisjak A, Tatone BSA, Mahabadi OK, Grasselli G, Marschall P, Lanyon GW, Re Vaissiere, Shao H, Leung H, Nussbaum C (2016) Hybrid finite-discrete element simulation of the EDZ formation and mechanical sealing process around a microtunnel in opalinus clay. *Rock Mech Rock Eng* 49:1849–1873
- Liu YS (2013) Brazilian splitting test theory and engineering application for anisotropic rock. Dissertation, Central South University, China
- Lockner D (1993) The role of acoustic emission in the study of rock fracture. *Int J Rock Mech Min Sci Geomech Abstr* 30:883–899
- Martin HR, Magnar NO, Jorn S, Erling F (2012) Static vs. dynamic behavior of shale. In: Bobet A (ed) 46th U.S. rock mechanics/geomechanics symposium, Chicago, USA
- Park B, Min KB (2015) Bonded-particle discrete element modeling of mechanical behavior of transversely isotropic rock. *Int J Rock Mech Min Sci* 76:243–255
- Pollock AA (2013) AE signal features: energy, signal strength, absolute energy and RMS (Rev. 1.2). Mistras Group INC, Minneapolis, pp 9–11
- Potyondy DO (2012) PFC 2D flat joint contact model. Itasca Consulting Group Inc, Minneapolis
- Potyondy DO, Cundall PA (2004) A bonded-particle model for rock. *Int J Rock Mech Min Sci* 41:1329–1364

- Roy DG, Singh TN (2016) Effect of heat treatment and layer orientation on the tensile strength of a crystalline rock under Brazilian test condition. *Rock Mech Rock Eng* 49:1–15
- Tan X, Konietzky H, Fruehwirt T, Dan DQ (2015) Brazilian tests on transversely isotropic rocks: laboratory testing and numerical simulations. *Rock Mech Rock Eng* 48:1341–1351
- Tavallali A, Vervoort A (2010) Effect of layer orientation on the failure of layered sandstone under Brazilian test conditions. *Int J Rock Mech Min Sci* 47:313–322
- Tsang CF, Barnichon JD, Birkholzer J, Li XL, Liu HH, Sillen X (2012) Coupled thermo-hydro-mechanical processes in the near field of a high-level radioactive waste repository in clay formations. *Int J Rock Mech Min Sci* 49:31–44
- Valente S, Fidelibus C, Loew S, Cravero M, Iabichino G, Barpi F (2012) Analysis of fracture mechanics tests on Opalinus Clay. *Rock Mech Rock Eng* 45:767–779
- Vallejos JA, Suzuki K, Brzovic A, Ivars DM (2016) Application of synthetic rock mass modeling to veined core-size samples. *Int J Rock Mech Min Sci* 81:47–61
- Vervoort A, Min KB, Konietzky H et al (2014) Failure of transversely isotropic rock under Brazilian test conditions. *Int J Rock Mech Min Sci* 70:343–352
- Wu SC, Xu XL (2016) A study of three intrinsic problems of the classic discrete element method using flat-joint model. *Rock Mech Rock Eng* 49:1813–1830
- Yang XX, Kulatilake PHSW, Jing HW, Yang SQ (2015a) Numerical simulation of a jointed rock block mechanical behavior adjacent to an underground excavation and comparison with physical model test results. *Tunn Undergr Space Technol* 50:129–142
- Yang ZP, He B, Xie LZ, Li CB, Wang J (2015b) Strength and failure modes of shale based on Brazilian test. *Rock Soil Mech* 36:3447–3464